scientific reports

OPEN

AI-powered prediction of hybrid nanofluid dynamics over a cylinder via LM optimized neural network approach

Muhammad Imran[1], Wantao Jia[1], Syed Tauseef Saeed[2], Jihad Younis[3]✉, Mubashir Qayyum[4] & Abdulrahman A. Almehizia[5]

This study examines the effect of chemical reaction and heat source/sink on steady two-dimensional mixed convective boundary layer flow of a hybrid nanofluid (HNF) over an inclined permeable plate/cylinder. The HNF is constructed by dispersing copper oxide (CuO) and titanium dioxide (TiO_2) nanoparticles in water (H_2O) as the base fluid. The model considers convective boundary conditions in both temperature and nanoparticle concentration. The resulting governing partial differential equations (PDEs) are reduced to a scheme of nonlinear ordinary differential equations (ODEs) via similarity transformations and numerically resolved by means of MATLAB's bvp4c solver. Originality of this paper deceptions in integrating a numerical solver with an optimized feed-forward artificial neural network (FF-ANN) based on the Levenberg–Marquardt algorithm (LMA) to model HNF flow along with heterogeneous and homogeneous chemical reactions, heat source/sink, and inclination effects, a combination rarely explored in previous studies. The results indicate that porosity and inclination parameters reduce the velocity profiles, while increased concentration of nanoparticles and heat source/sink effect enhance thermal distribution. The LMA-ANN model possesses good predictive ability with the mean squared error (MSE) varying between 10^{-08} and 10^{-10}. There is excessive consistency among the numerical solutions, as presented. The outcomes showcase the huge potential of HNFs and ANN-enhanced modeling to boost heat and mass transfer in complex engineering and industrial operations.

Keywords Hybrid nanofluid, Cylinder/plate, Chemical reaction, bvp4c method, Artificial neural network, Levenberg–Marquardt algorithm

List of symbols

u	Axial velocity component, m/s
v	Radial velocity component, m/s
η	Similarity variable
f	Dimensionless stream function
f'	Dimensionless velocity profile
θ	Dimensionless temperature profile
ϕ	Dimensionless concentration profile
β_T	Thermal Biot number
δ	Curvature factor
T_s	Cylinder surface temperature, K
T_p	Plate surface temperature, K
T_∞	Ambient temperature, K

[1]School of Mathematics and Statistics, Northwestern Polytechnical University, Xi'an 710072, China. [2]Department of Mathematics and Statistics, The University of Lahore, Lahore, Pakistan. [3]Department of Mathematics, Aden University, Aden, Yemen. [4]Department of Sciences and Humanities, National University of Computer and Emerging Sciences, Lahore, Pakistan. [5]Drug Exploration and Development Chair (DEDC), Department of Pharmaceutical Chemistry, College of Pharmacy, King Saud University, 11451 Riyadh, Saudi Arabia. ✉email: jihadalsaqqaf@gmail.com

λ	Mixed convection parameter
φ	Porosity factor
$\Pr$	Prandtl number
Q	Heat source/sink parameter, W/m^3
Gr	Grashof number
Rd	Thermal radiation parameter
D_m	Mass diffusion coefficient, m^2/s
k_h	Homogeneous reaction rate constant, s^{-1}
k_{het}	Heterogeneous reaction rate constant, s^{-1}
Sc	Schmidt number
Le	Lewis number
Re	Reynolds number
Pe	Peclet number
Nu	Nusselt number
Sh	Sherwood number
Ω	Angular velocity, rad/s
ρ	Base fluid density, kg/m^3
ρ_{nf}	Nanofluid density, kg/m^3
ρ_{hnf}	Hybrid nanofluid density, kg/m^3
C_p	Specific heat at constant pressure, J/kg K
K	Thermal conductivity, W/m K
μ	Dynamic viscosity, Pa s
μ_{nf}	Nanofluid viscosity, Pa s
μ_{hnf}	Hybrid nanofluid viscosity, Pa s
σ	Electrical conductivity, S/m
σ^*	Stefan–Boltzmann constant, W/m^2 K^4
τ	Ratio of nanoparticle to fluid heat capacity

Research background

Researchers are looking at the prospect of utilizing microscopic fluids to boost heat transmission, with a particular emphasis on solar collectors. It is insufficient to enhance heat transmission to employ common fluids like ethylene glycol, candle oil, drinking water, and other similar materials. Scholars have researched to advance the rate of heat transmission. After that, they concluded that the main causes of the observed decline in growing mass and heat transfer rates are breakdown and obstruction. Nanofluids are used to mitigate these issues. Actually, fluids with scattered small particles likely particles ranging in size from one to one hundred nanometers were referred to as "nanofluid" by Choi[1]. These nanoparticles are suspended in certain base fluids. The creation of more effective heat transfer methods is the primary obstacle confronting the younger researchers in this field. The majority of upgrading procedures may be divided into two groups. This has to do with certain latent and dynamic strategies. Certain calculations, liquid additives, hot pressing, and other procedures are required for specialized latent processes. External powers are required for dynamic methods that use electric and magnetic fields.

The majority of upgrading procedures fall into one of two types and employ liquid addition chemicals to upsurge thermal routine of common fluids, such as water, oil, and ethylene -glycol mixtures. This has to do with certain latent and dynamic strategies. Certain calculations, liquid additives, hot pressing, and other procedures are required for specialized latent processes. External powers are required for dynamic methods that use electric and magnetic fields. Liquid additive chemicals are used to boost heat transmission quality of common fluids, such as water and oil mixtures, by Hayat et al.[2]. Many researchers have thoroughly examined the effect of a powerful fluid mixture over crucial heat transfer enrichment. It has been observed that the combination was improperly used to upgrade thermal execution due to a variety of circumstances, such as blockage, abrasion, additional pressure loss, etc. All of these issues have been resolved by nanofluids, which also provide some highly noteworthy benefits, including uniformity, long-term strength, little pausing in stream segments, and good heat conductivity at lower nanoparticle concentrations. These materials' special properties make them valuable in a variety of fields, including healthcare and industry. Buongiorno et al.[3] investigated Brownian motion's special sliding characteristics and thermophoresis development around the nanofluid. Madhukesh et al.[4] explored the thermal transport analysis of ternary hybrid nanofluid flow along a vertical cylinder, including thermal radiation and chemical reactions. Numerous writers, including Yaswin et al.[5], Gupta et al.[6], Salahuddin et al.[7], Chinnaswamy et al.[8], and Saha et al.[9], conducted comparable study analyses.

Literature analysis

Nanofluids possess high thermal conductivity than conventional fluids with better heat transfer efficiency. Among those, hybrid nanofluids constructed by suspending two or extra nanoparticles in a base fluid are attracting the attention of researchers due to their high thermal characteristics. These fluids are increasingly being applied in areas such as solar energy collection, transformer cooling, microscale technologies, and automotive systems, with additional applications illustrated in Fig. 1. The selection of suitable nanoparticle combinations is essential for maintaining suspension stability in hybrid nanofluids. Commonly used nanoparticles include metals (Cu, Ag), metal oxides (GO–Fe_2O_3), and carbon-based materials like graphite and carbon nanotubes (CNTs). Due to their superior thermal conductivity, hybrid nanofluids outperform single-particle nanofluids, making them promising for widespread industrial use. Their efficiency contributes to higher system performance, reduced energy consumption, and overall cost savings. These advantages have attracted considerable research interest in

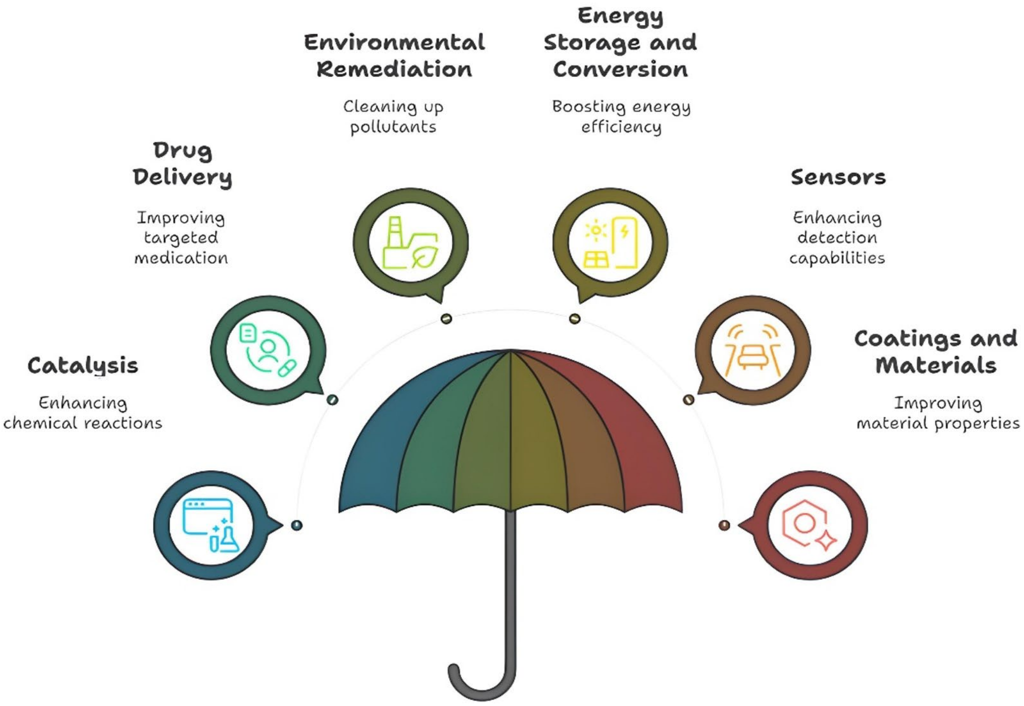

Fig. 1. Applications of hybrid nanoparticles.

recent years. Upreti et al.[10] observed impacts of thermodynamics and heat transfer studies on stream of fascinated Casson HNF across a Riga plate, including thermal radiation. Wang et al.[11] examined the unsteady thermal transport stream of Casson nanofluids using the generalized Mittag–Leffler kernel of Prabhakar's kind. Wang et al.[12] provide insights into the concentration fluctuations associated with leading-edge accretion and thermal analysis including water-based nanotubes, graphene, and aluminum oxide nanoparticles on a convectively heated surface. Fuzhang et al.[13] investigated inspections of an unbalanced micropolar nanofluid model along an exponentially spreading curved surface with a chemical reaction. Ramesh et al.[14] investigated HNF via a permeable cylinder considering homogeneous-heterogeneous reactions and slip effects.

Stretching and rotating cylinders play a significant role in an assortment of engineering applications, containing wire drawing, thermal imprinting, and the mitigation of fluid drag. The alternation of cylinder notably influences surrounding vortex behavior, often diminishing vortex shedding, as supported by numerous studies. For instance, Wei et al.[15] discussed the substrate-less power semiconductor packaging for the potential of recyclability. Additionally, Qi et al.[16] considered the novel thermal error control strategy for feed drive mechanisms via sintered core heat pipe-cooled moving nut. Qian[17] investigate the numerical characterization and formation process study of rail light bands in high-speed turnout areas.

The escalating demand for efficient thermal management across various technological sectors, such as nuclear energy, electronics, purification processes, chemical apparatuses, automotive systems, and crude oil heating, has underscored the importance of enhanced heat transfer mechanisms. In this context, the incorporation of heat sources and sinks significantly influences the flow behavior and thermal performance of nanofluids. Rawat et al.[18] examine the importance of nanoparticle aggregation and the effects of a non-uniform heat source/sink on the flow of titania–ethylene glycol nanofluid across a wedge. Dinarvand et al.[19] investigated the squeezing flow of aqueous CNTs-Fe_3O_4 hybrid nanofluid using a mass-based method, focusing on the effects of heat source/sink, nanoparticle morphology, and an oblique magnetic field. Aslani et al.[20] examined the influence of partial slip and radiation on liquid film fluid flow across an unstable porous stretched sheet, including viscous dissipation and heat source/sink effects. Reddappa et al.[21] investigated the impact of second-order chemical reactions on MHD forced convection of Cu, Ag, and Fe_3O_4 nanoparticles in Jeffrey nanofluid across a moving plate inside a porous media, considering the existence of heat sources and sinks. For instance, Al-Shammari et al.[22] investigated the effects of heat sources and sinks on gravity-driven flows, analyzing the amplitude variations in thermal and concentration boundary layers. Their study also delved into how varying inclination angles affect shear stress, as well as oscillatory nature of heat and mass relocation rates.

ANNs have proven to be highly effective tools in the field of fluid dynamics. As a subset of machine learning, ANNs are designed to detect intricate patterns and relationships within data, as noted by Mandal et al.[23]. They have been successfully applied to a range of fluid dynamics problems, such as flow prediction, turbulence modeling, and control strategies, as highlighted by Seawram et al.[24]. Ramesh et al.[25] examined neural network techniques for a curved riga sensor in a ternary HNF including chemical reactions and Arrhenius kinetics. Unlike these conventional approaches, ANNs can capture input–output relationships directly from data, eliminating the need for predefined governing equations. Drawing stimulation from the human brain's neural structure, ANNs are accomplished of learning, adapting, and executing complex computational chores. Kumar et al.[26] developed an artificial neural network technique for the time-dependent radiative flow of Casson fluid with couple stresses in a microchannel. Galal et al.[27] investigated a Bayesian regularization neural network methodology for predicting the spread of the hepatitis B virus and modeling protected system treatment. Butt et al.[28] investigated MHD slip movement in nanofluids for thermal energy stowage in astrophysical collectors, including radiation and conductivity belongings via a unique strategy using a successive quadratic programming-based neuro-evolutionary technique. Additionally, several types of neural network architectures, including feedforward, recurrent, radial basis function, wavelet-based, and finite element neural networks, have been explored for solving differential equations in various fluid mechanics contexts.

Feedforward Neural Networks (FFNNs) are esteemed for their adaptability, robust representational power, and effectiveness across diverse learning applications examined by Lee, H., & Kang, I. S.[29]. Their proficiency in function approximation renders them particularly advantageous for resolving ODEs and PDEs discussed by Lagaris et al.[30]. Qureshi et al.[31] spoke about employing ANNs for machine learning-based stochastic analysis of heat and momentum transfer in ternary-HNFs with aggregation properties. Similarly, Srinivasacharya and Sarwan[32] applied ANN modeling to assess inspiration of Dufour and Soret effects on Casson fluid stream over an unstable sheet experiencing radial extension, thereby cultivating empathetic of heat and mass allocation in such structures. AI-driven investigation of buoyancy-convective flow of ternary-hybrid nanofluid in a porous media across a stretched cylinder was enclosed by Qureshi et al.[33]. Ravi and Kaladhar[34] employed Levenberg–Marquardt method to investigate mixed convection stream of a Jeffrey fluid among two revolving disks under combined effects of a magnetic field also thermal contamination, providing valuable information on the thermal and flow behavior of such configurations. An ANN-driven study of heat exchange using a polymer/CNT hybrid nanofluid between parallel sheets was covered by Qureshi et al.[35]. Furthermore, Butt et al.[36] utilized ANNs in conjunction with radial basis purposes to examine the 2D MHD stream of a Williamson nanofluid on stretching sheet, demonstrating the applicability of these computational techniques in analyzing non-Newtonian fluid flows.

Novelty of the work

We noticed from the previously indicated study that several investigations, especially hybrid ones, were based on intellect examinations of nanofluid movement. Furthermore, before implementing the existing structure and approach, the study on the effects employed in the inquiry was not considered. This study aims to examine how chemical reaction & heat source/sink affect the mixed convection of hybrid nanofluid flow over a permeable plate/cylinder. The primary purpose of this research will be achieved by conducting this inspection. Although water (H_2O) comprises copper oxide (CuO) and titanium dioxide (TiO_2) nanoparticles, it is still considered a conventional fluid. The numerical approach utilizes an FF-ANN based LMA, which is used to simplify the computation of the resultant governing system of equations. On graphical identity, the impacts of various physical properties, such as Heat capacity, density, and thermal radiation, on velocity, temperature, and mass profile are seen. The key novelties are given as follows:

- Dual-nanoparticle Hybrid Nanofluid Composition CuO–TiO_2 used in water as a hybrid nanofluid with augmented thermal conductivity above single nanoparticle theory.
- Mixed Convection over a Porous Cylinder/Plate: Geometry is new and industrially applicable, being closer to realistic boundary conditions than flat plates.
- Incorporation of Chemical Reaction and Heat Source/Sink: Simultaneous simulation of thermal and mass transfer complexities, including realistic industrial and biological processes.
- Hybrid Computational Approach: Interfacing of classic numerical method (bvp4c) with feed-forward ANN (FF-ANN) using LM-optimization for forecasting and performance improvement.
- Convective Boundary Conditions for Temperature and Concentration: A non-standard boundary condition setup reflecting complex surface-fluid interactions, which are often ignored in similar research.
- Low MSE Verification of ANN Predictions: Demonstrates the capability of machine learning to reproduce complex physics-based systems within an acceptable error threshold.

Mathematical formulation

Study examines 2D laminar HNF flow across a permeable inclined plate/cylinder with mixed convection and heat source/sink. Copper oxide (CuO) and titanium dioxide (TiO_2) nanoparticles are utilized in water (H_2O) to produce HNF. Axial and radial orders are shown by x, y and r, individually, while u represents the reference velocity (Fig. 2 shows fluid flow over the geometry). The ambient and surface temperatures of the plate and cylinder are represented by T_∞ and T_w, respectively. Exterior forces and pressure gradients are presumed not to affect nanofluid flow.

The nanofluid model assumes both heterogeneous and homogeneous reactions between chemical components A^* and B^*. This model considers a cubic homogeneous response inside the boundary layer flow. Pooja, Narasimhamurthy, and Anitha[37] report a first-order heterogeneous reaction over catalyst surface.

$$\begin{aligned} &A^* + 2B^* \rightarrow 3B^*, \qquad rate = l_1 ab^2, \\ &A^* \rightarrow B^*, \qquad\qquad\quad rate = l_s a. \end{aligned}$$

Chemical species absorptions A^* and B^* are denoted by a and b, respectively, whereas l_1 and l_s represent constant rate. The modeled equations based on following assumptions are formulated as Madhukesh et al.[38]. And Pooja, Narasimhamurthy, and Anitha[37]: To obtain the governing equations, the flow is characterized under

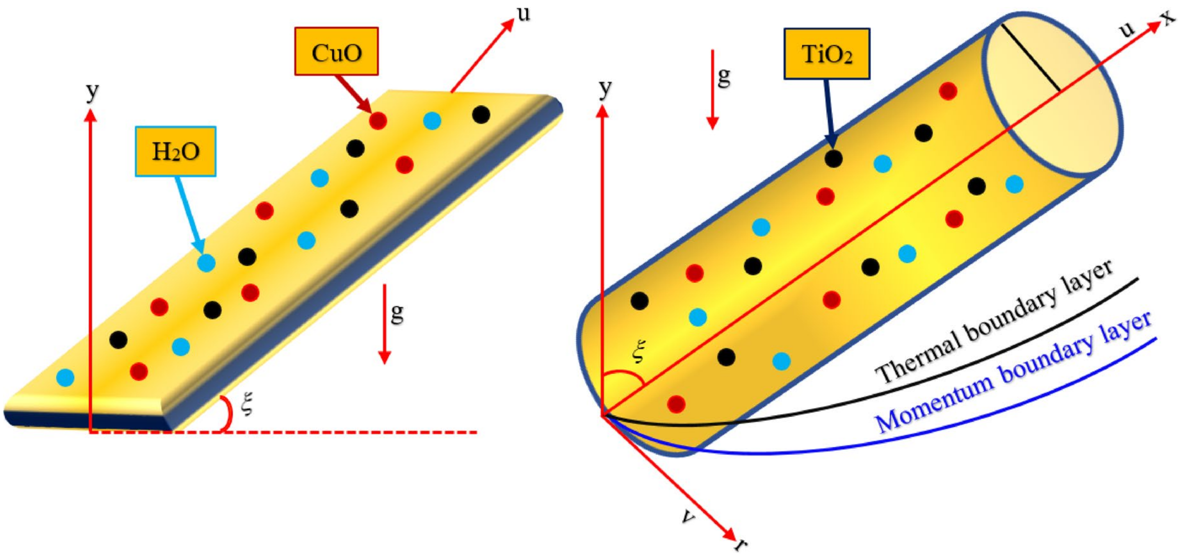

Fig. 2. Fluid flow over plate/cylinder.

some physical assumptions to simplify the problem but with a assurance of accuracy. The analysis considers a boundary layer command where velocity and temperature gradients in the direction across the surface are dominant. Longitudinal pressure gradients and external forces are excluded since buoyancy, viscous stresses, and convective influences are dominant in the current configuration[4,10,13]. In addition, the dual-nanoparticle hybrid nanofluid is selected by its enhanced thermal conductivity and better heat transfer properties as reported in recent research[12,19]. Positive values of dimensionless parameters, i.e., Prandtl number (Pr), Schmidt number (Sc), and Lewis number (Le), are imposed to ensure the solutions are thermophysically feasible[22,27]. These assumptions have a logical physical basis for the mathematical modeling.

$$\frac{\partial\left(ru\right)}{\partial x}+\frac{\partial\left(ru\right)}{\partial r}=0, \tag{1}$$

$$u\frac{\partial\left(u\right)}{\partial x}+v\frac{\partial\left(u\right)}{\partial r}=\upsilon_{hnf}\left(\frac{\partial^{2}u}{\partial r^{2}}+\frac{1}{r}\frac{\partial u}{\partial r}\right)+\frac{\left(\rho\beta\right)_{hnf}g\left(T_{1}-T_{\infty}\right)\cos\vartheta}{\rho_{hnf}}-\frac{\upsilon_{hnf}}{K_{1}^{*}}u, \tag{2}$$

$$\begin{gathered}u\frac{\partial\left(T\right)}{\partial x}+v\frac{\partial\left(T\right)}{\partial r}=\\ \alpha_{hnf}\left(\frac{\partial^{2}T}{\partial r^{2}}+\frac{1}{r}\frac{\partial T}{\partial r}\right)-\frac{1}{\left(\rho C_{p}\right)_{hnf}}\frac{\partial}{\partial y}\left(q_{r}\right)+\frac{Q_{e}^{*}}{\left(\rho C_{p}\right)_{hnf}}\left(T-T_{\infty}\right)\exp\left(-\sqrt{\frac{a}{\upsilon_{f}}}ny\right),\end{gathered} \tag{3}$$

$$u\frac{\partial a}{\partial x}+v\frac{\partial a}{\partial r}=D_{A}\left(\frac{\partial^{2}a}{\partial r^{2}}+\frac{1}{r}\frac{\partial a}{\partial r}\right)-l_{1}ab^{2}, \tag{4}$$

$$u\frac{\partial b}{\partial x}+v\frac{\partial b}{\partial r}=D_{B}\left(\frac{\partial^{2}b}{\partial r^{2}}+\frac{1}{r}\frac{\partial b}{\partial r}\right)-l_{1}ab^{2}, \tag{5}$$

Equation (3) defines q_r as (Mahmood, Rafique, Khan, et al.[39]):

$$q_{r}=-\frac{4\sigma^{*}}{3k^{*}}\frac{\partial}{\partial y}\left(T^{4}\right). \tag{6}$$

Energy equation converted:

$$\begin{gathered}u\frac{\partial\left(T\right)}{\partial x}+v\frac{\partial\left(T\right)}{\partial r}=\\ \alpha_{hnf}\left(\frac{\partial^{2}T}{\partial r^{2}}+\frac{1}{r}\frac{\partial T}{\partial r}\right)-\frac{1}{\left(\rho C_{p}\right)_{hnf}}\frac{16\sigma^{*}}{3k^{*}}T_{h}^{3}\frac{\partial^{2}T}{\partial y^{2}}+\frac{Q_{e}^{*}}{\left(\rho C_{p}\right)_{hnf}}\left(T-T_{\infty}\right)\exp\left(-\sqrt{\frac{a}{\upsilon_{f}}}ny\right),\end{gathered} \tag{7}$$

Boundary conditions (BCs) are as follows (Madhukesh et al.[38]):

$$\left.\begin{array}{c} u = u_w = \frac{U_0^* x}{l},\ v = 0,\ -k\frac{\partial r}{\partial T} = h_f\left(T_w - T\right),\ D_A\frac{\partial a}{\partial r} = l_s a,\ D_B\frac{\partial B}{\partial r} = l_s a \\ at\ r = R,\ \ u \to 0,\ T \to T_\infty,\ a \to a_0,\ b \to 0,\ r \to \infty \end{array}\right\} \tag{8}$$

The applied convective thermal boundary conditions depict authentic industrial and biological situations in which heat transfer transpires by convection instead of sustaining a constant wall temperature. The concentration boundary conditions model also regulated the injection or absorption of nanoparticles at the surface, which is common in cooling, coating, and energy systems that use nanofluids[12,19,27]. Consider the exponentially space-based heat source/sink term in Eq. (7), In order to more accurately represent thermal systems in real life, the model requires a heat source/sink that is increasingly space-based, as the absorption and emission of heat are location-dependent. The inconsistent thermal distribution is captured by this method. Which is crucial for the comprehension and enhancement of thermal efficiency and disturbance in nanofluid fluxes in real-world submissions such as energy schemes and electronics cooling systems that necessitate precise thermal control. The similarity variables are as follows by Madhukesh et al.[38]:

$$\left.\begin{array}{c} \psi = \sqrt{u_w v_f x} R f\left(\xi\right),\ \theta = \frac{T - T_\infty}{T_w - T_\infty},\ u = \frac{1}{r}\frac{\partial \psi}{\partial r},\ v = -\frac{1}{r}\frac{\partial \psi}{\partial x} \\ h\left(\xi\right) = \frac{b}{a_0},\ g\left(\xi\right) = \frac{b}{a_0},\ \xi = \sqrt{\frac{u_w}{v_f x}}\left(\frac{r^2 - R^2}{2R}\right). \end{array}\right\} \tag{9}$$

By applying Eq. (9) to Eqs. (1–5) and (8), the modeled equations become:

$$\frac{\left(\left(1 + \left(2\delta\right)\xi\right) f''' + \left(2\delta\right) f''\right)}{B_1 B_2} - \left(f'\right)^2 - \frac{P_m}{B_1 B_2} f' + f f'' + \frac{B_3}{B_2}\gamma\theta\cos\vartheta = 0, \tag{10}$$

$$\left(1 + Rd\frac{k_{hnf}}{k_f P_r B_4}\right)\left(\left(1 + 2\delta\xi\right)\theta'' + 2\delta\theta'\right) + f\theta' + Q_e \exp\left(-n\xi\right) = 0. \tag{11}$$

$$\left(1 + 2\delta\xi\right) h'' + \delta h' + Scfh' - ScL_1 hg^2 = 0. \tag{12}$$

$$\alpha\left(1 + 2\delta\xi\right) g'' + \delta\alpha g' + Scfg' - ScL_1 hg^2 = 0. \tag{13}$$

The BCs for ODEs are:

$$\left.\begin{array}{c} f\left(\xi\right) = 0,\ f'\left(\xi\right) = 1,\ \theta'\left(\xi\right) = -\lambda\left(1 + \theta\left(\xi\right)\right),\ h'\left(\xi\right) = L_s h\left(0\right),\ \alpha g'\left(0\right) = -L_s h\left(0\right) \\ at\ \xi = 0,\ f'\left(\infty\right) = 0,\ \theta\left(\infty\right) = 0,\ h\left(\infty\right) \to 1,\ g\left(\infty\right) \to 0\ as\ \xi \to 0 \end{array}\right\} \tag{14}$$

Table 1 shows physical parameters, including symbols and expressions (Madhukesh et al.[38]; Pooja, Narasimhamurthy, and Anitha[37]).

In the current situation, each of the dimensionless characteristics in Table 1 has its own physical meaning. For example, Prandtl number (Pr) is the ratio of momentum diffusivity to thermal diffusivity. It also controls how thick velocity and thermal boundary layers are compared to each other. The Lewis number (L_e) shows how fast heat and mass diffuse relative to one other, and the Schmidt number (Sc) shows how fast momentum diffuses compared to mass, which affects the concentration gradients of nanoparticles. The mixed convection parameter (γ) shows how strong buoyancy-induced natural convection is compared to forced convection. The heat source/sink parameter (Q_e) shows how thermal energy is generated or absorbed within the system. The porosity factor (P_m) and curvature parameter (δ) also show how the porous medium resists flow and how the plate or cylinder affects the shape of the medium. Clarifying these physical functions enhances the connection between mathematical modelling and the actual physical system being examined.

Where

$$B_1 = \frac{\mu_{hnf}}{\mu_{bf}},\ B_2 = \frac{\rho_{hnf}}{\rho_{bf}},\ B_3 = \frac{\left(\rho\beta\right)_{hnf}}{\left(\rho\beta\right)_{bf}},\ B_4 = \frac{\left(\rho C_p\right)_{hnf}}{\left(\rho C_p\right)_{bf}},\ B_5 = \frac{k_{hnf}}{k_{bf}},\ B_6 = \frac{\sigma_{hnf}}{\sigma_{bf}}. \tag{15}$$

Tables 2 provides numerical standards of thermophysical parameters of nanoparticles and the base fluid. The expressions for skin friction and Nusselt number, together with their transformed forms, are as follows:

$$\left.\begin{array}{c} C_f = \left.\frac{\partial u}{\partial r}\right|_{r=R}\left(\frac{\mu_{hnf}}{\rho_f u w^2}\right),\ N_u = \left.\frac{\partial T}{\partial r}\right|_{r=R}\left(\frac{-x k_{hnf}}{k_f\left(T_w - T_\infty\right)}\right), \\ C_f = \frac{f''(0)}{B_1(\mathrm{Re})^{0.5}},\ Nu = \frac{-\left(k_{hnf} + R_d\right)(\mathrm{Re})^{0.5}}{k_f}\theta'\left(0\right). \end{array}\right\} \tag{16}$$

Thermophysical properties

The thermophysical characteristics of nanoparticles significantly influence thermal conductivity and heat transfer efficiency in nanofluids. The efficiency of heat transport inside a structure is dictated by specific heat capacity, thermal conductivity, and density. Thermal conductivity increases as the fluid's heat-conductive properties enhance, while specific heat capacity delineates the quantity of heat energy that may be retained. Viscosity and density influence fluid flow, since elevated viscosity may diminish efficiency by necessitating more power for pumping. In natural convection, the thermal expansion coefficient facilitates heat transport in certain applications.

Physical parameter	**Symbols**	**Expressions**
Thermal Biot number	λ	$\lambda = h_f \sqrt{\frac{v}{U_0^*}}$
Curvature factor	δ	$\delta = \sqrt{\frac{v_f}{U_0^* R^2}}$
Cylinder surface	$\delta > 0$	
Plate surface	$\delta = 0$	
Mixed convection factor	γ	$\gamma = \frac{Gr}{\mathrm{Re}^2} = \frac{g\beta(T_w - T_\infty)}{u_w U_0^*}$
Porosity factor	P_m	$P_m = \frac{v_f}{U_0^* K^*}$
Prandtl number	Pr	$\mathrm{Pr} = \frac{v_f}{\alpha_f^*}$
Heat source/sink constraint	Q_e	$Q_e = \frac{Q_e^*}{a(\rho C_p)_f}$
Grashof number	Gr	$Gr = \frac{g\beta(T_w - T_\infty)^3}{v_f^2}$
Thermal radiation constant	R_d	$R_d = \frac{16\sigma^* T_h^3}{3k^* k_f}$
Mass diffusion coefficient	α	$\alpha = \frac{D_A}{D_B}$
Homogeneous reaction parameter	L_1	$L_1 = \frac{a_0^2}{U}$
Heterogeneous reaction parameter	L_s	$L_s = \frac{1}{D_A} \sqrt{\frac{v}{U}}$
Schmidt number	Sc	$Sc = \frac{v}{D_A}$

Table 1. Physical parameters, symbols and expressions.

Physical properties	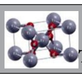 **TiO_2**	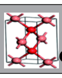 **CuO**	 **H_2O**
$\rho \left(kg/m^3\right)$	4250	6320	997.1
$k\ (W/mK)$	8.9538	76.500	0.6130
$C_p\ (J/kgK)$	686.2	531.8	4179

Table 2. Numerical values of thermophysical properties.

Furthermore, in electromagnetic devices, the electrical and magnetic characteristics of nanoparticles may be used to enhance heat transfer regulation. Through the optimization and meticulous selection of these features, nanofluids may markedly enhance the thermal system performance across many engineering applications. Table 3 illustrates the thermophysical characteristics of the relevant particles. The spherical nanoparticle assumptions on which the correlations of effective properties employed here rely are typical of the majority of nanofluid studies in the literature[12,19,27]. Although real nanoparticles such as CuO and TiO_2 are generally non-spherical or lattice type, the spherical assumption is convenient to make for modeling and a fair representation for capturing the primary heat and mass transfer behavior. The influence of lattice morphology and anisotropic particle shape, though important, lies outside the scope of this work and will be treated in future studies.

Graphical representations of thermophysical properties

Below the Figs. 3, 4 and 5 are the explanations of thermophysical possessions of nanoparticles (CuO, TiO_2) and base fluid Water (H_2O), as detailed in references[40,41]. These properties are crucial as far as establishing heat and mass transfer characteristics of the nanofluid system is concerned. Thermal conductivity, specific heat capacity, and density are all factors that directly influence the effectiveness of heat transfer as well as the flow behavior of the system. Accurate modeling of these materials is essential to obtain realistic simulation results and in order to accurately include them in numerical and neural network models.

Methodology

This part describes numerical technique utilized in the work, based on an extended ODEs model. Figure 6 illustrates the general procedure. The paper conducts an extended computational investigation of dynamics of heat transfer in MHD Casson HNF flow, with water as the base fluid, over a vertically stretching sheet. The bvp4c solver in MATLAB is combined with ANNs for accurate simulations. The initial mesh contained 50–100

Properties	Hybrid Nano fluid
Viscosity	$\frac{\mu_{hnf}}{\mu_{bf}} = \frac{1}{\left(1-\phi_{TiO_2}-\phi_{CuO}\right)^2}$
Density	$\frac{\rho_{hnf}}{\rho_{bf}} = \phi_{TiO_2}\left(\frac{\rho_{TiO_2}}{\rho_{bf}}\right) + \phi_{CuO}\left(\frac{\rho_{CuO}}{\rho_{bf}}\right) + \left(1-\phi_{TiO_2}-\phi_{CuO}\right)$
Electrical conductivity	$\frac{\sigma_{hnf}}{\sigma_{bf}} = \left[\frac{\left(\frac{\phi_{TiO_2}\sigma_{TiO_2}+\phi_{CuO}\sigma_{CuO}}{\phi_{TiO_2}+\phi_{CuO}}\right)+2\sigma_{bf}+2\left(\phi_{TiO_2}\sigma_{TiO_2}+\phi_{CuO}\sigma_{CuO}\right)-2\left(\phi_{TiO_2}+\phi_{CuO}\right)\sigma_{bf}}{\left(\frac{\phi_{TiO_2}\sigma_{TiO_2}+\phi_{CuO}\sigma_{CuO}}{\phi_{TiO_2}+\phi_{CuO}}\right)+2\sigma_{bf}-2\left(\phi_{TiO_2}\sigma_{TiO_2}+\phi_{CuO}\sigma_{CuO}\right)+2\left(\phi_{TiO_2}+\phi_{CuO}\right)\sigma_{bf}}\right]$
Heat capacity	$\frac{(\rho C_p)_{hnf}}{(\rho C_p)_{bf}} = \phi_{TiO_2}\left(\frac{(\rho C_p)_{TiO_2}}{(\rho C_p)_{bf}}\right) + \phi_{CuO}\left(\frac{(\rho C_p)_{CuO}}{(\rho C_p)_{bf}}\right) + \left(1-\phi_{TiO_2}-\phi_{CuO}\right)$
Thermal conductivity	$\frac{k_{hnf}}{k_{bf}} = \left[\frac{\left(\frac{\phi_{TiO_2}k_{TiO_2}+\phi_{CuO}k_{CuO}}{\phi_{TiO_2}+\phi_{CuO}}\right)+2k_{bf}+2\left(\phi_{TiO_2}k_{TiO_2}+\phi_{CuO}k_{CuO}\right)-2\left(\phi_{TiO_2}+\phi_{CuO}\right)k_{bf}}{\left(\frac{\phi_{TiO_2}k_{TiO_2}+\phi_{CuO}k_{CuO}}{\phi_{TiO_2}+\phi_{CuO}}\right)+2k_{bf}-2\left(\phi_{TiO_2}k_{TiO_2}+\phi_{CuO}k_{CuO}\right)+2\left(\phi_{TiO_2}+\phi_{CuO}\right)k_{bf}}\right]$

Table 3. Thermo-physical attributes of hybrid nano fluid.

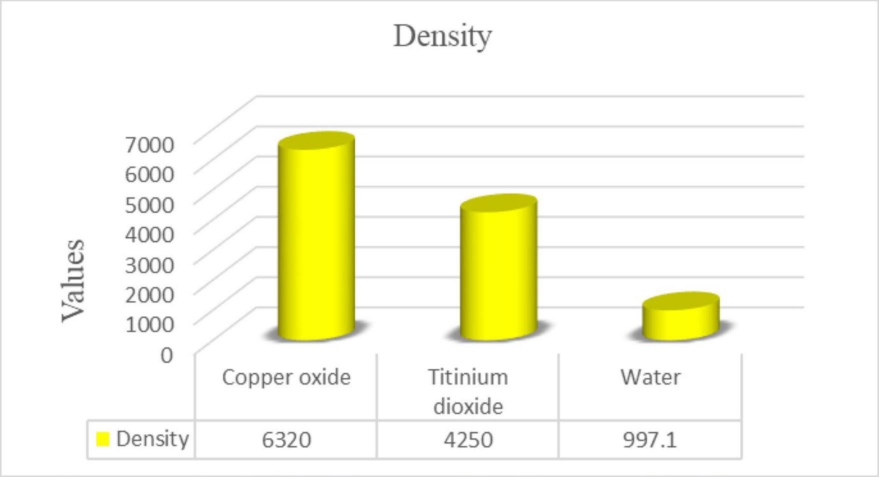

Fig. 3. Density of concerned nanoparticles.

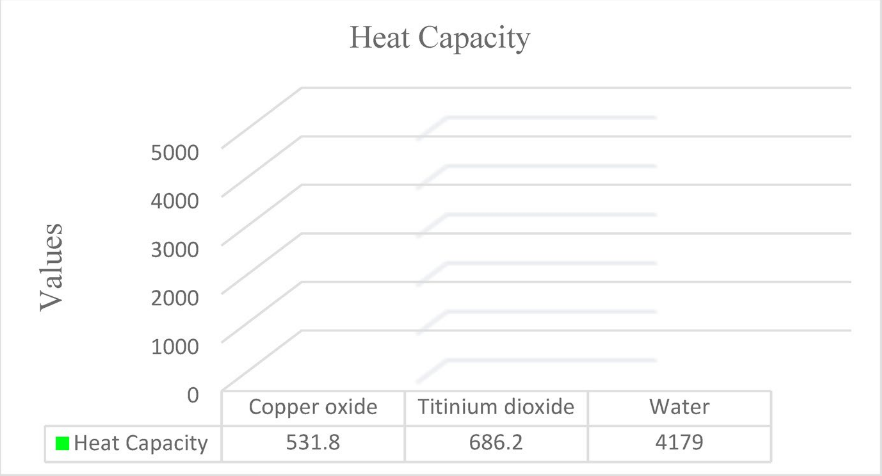

Fig. 4. Heat capacity of deliberated nanoparticles.

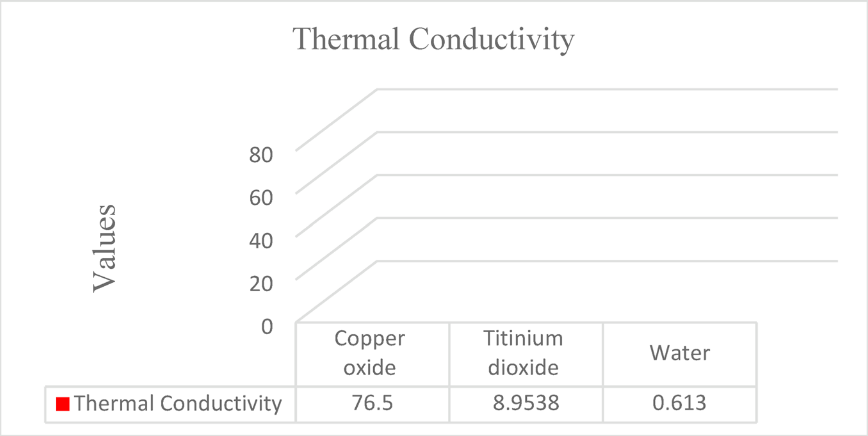

Fig. 5. Thermal conductivity of discussed nanoparticles.

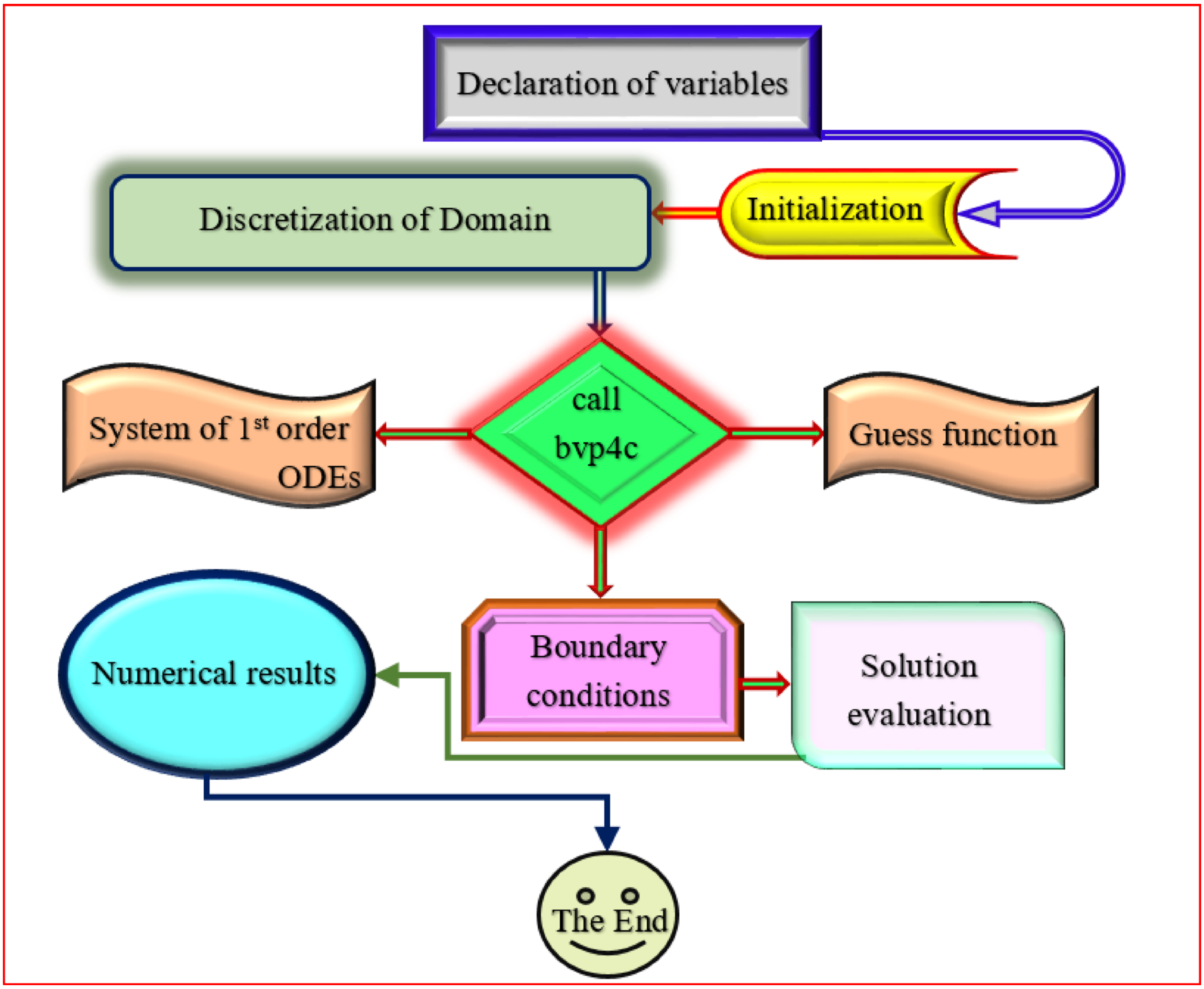

Fig. 6. Methodology flow chart.

points and was adaptively refined by bvp4c during iteration. Convergence was assured by monitoring successive solutions through negligible differences in profiles. The semi-infinite boundary condition was checked by extending the computational domain beyond $\eta = 5$ to verify solution invariance.

Numerical scheme

This section delineates numerical resolution of arrangement of ODEs via RK-4 method, accompanied by the pertinent boundary conditions. The graphs reveal minimal variation in fluid movement behavior when the standards were equal to or exceeded 5. Consequently, the domain for a specific problem will be considered as [0, 5] rather than [0, ∞]. For this work, the ANN architecture consisted of two hidden layers containing 11 neurons with sigmoid transfer function and an output layer containing nine neurons for velocity, temperature, and concentration profiles. The bvp4c data was divided into 80% training data, 10% validation, and 10% testing. The bvp4c solver was run with RelTol = 1×10^{-7} and AbsTol = 1×10^{-9}, while the ANN training reached an MSE of order 10^{-6}–10^{-7} with R≈0.999. To facilitate this, we convert the ordinary differential equations, along with their boundary conditions, into first-order equations as illustrated below:

$$\begin{gathered} t_1 = f, t_2 = f', t_3 = f'', t_3' = f''', \\ t_4 = \theta, t_5 = \theta', t_5' = \theta'', \\ t_6 = h, t_7 = h', t_7' = h'', \\ t_8 = g,\ t_9 = g',\ t_9' = g'' \end{gathered} \tag{17}$$

$$t_3' = \frac{B_1 B_2 t_2^2 + P_m t_2 - B_1 B_2 t_1 t_3 - (2\delta)\, t_3 - B_1 B_3 \gamma \cos\vartheta t_4}{(1 + (2\delta)\,\xi)}, \tag{18}$$

$$t_5' = -\frac{k_f P_r B_4}{(k_f P_r B_4 + k_{hnf} Rd)\,(1 + 2\delta\xi)} \left\{ \left(1 + Rd \frac{k_{hnf}}{k_f P_r B_4} \right) 2\delta t_5 + t_1 t_5 + Q_e \exp(-n\xi) \right\}. \tag{19}$$

$$t_7' = \frac{ScL_1 t_6 t_8^2 - \delta t_7 - Sct_1 t_7}{(1 + 2\delta\xi)}. \tag{20}$$

$$t_9' = \frac{ScL_1 t_6 t_8^2 - \delta\alpha t_9 - Sct_1 t_9}{\alpha\,(1 + 2\delta\xi)}. \tag{21}$$

$$\left. \begin{array}{c} t_1(\xi) = 0,\ t_2(\xi) = 1,\ t_5(\xi) = -\lambda\,(1 + t_4(\xi)),\ t_7(\xi) = L_s t_6(0),\ \alpha t_9(0) = -L_s t_6(0) \\ at\ \xi = 0,\ t_2(\infty) = 0,\ t_4(\infty) = 0,\ t_6(\infty) \to 1,\ t_8(\infty) \to 0\ as\ \xi \to 0 \end{array} \right\} \tag{22}$$

Framework of artificial neural networks (AANs)

ANNs consist of multiple organized processing units, or neurons, prearranged into layers. In an FNN, data flows unidirectionally from the input layer through one or more hidden layers to the output layer. The input layer receives the data, hidden layers process it through weighted connections and activation functions, and the output layer produces the final result. Each layer learns specific weights during the training process to minimize error among predicted and actual outputs. ANNs are particularly effective in modeling complex nonlinear relationships due to their ability to adjust internal parameters and approximate functions across diverse datasets. Activation functions introduce nonlinearity into network, permitting it to capture intricate patterns between inputs and outputs, a capability supported by universal approximation theorem, which states that a FFN with at least one hidden layer can approximate any incessant function on compact subsets of R^n, given appropriate activation functions. Designing an optimal ANN architecture involves selecting the appropriate number of neurons, hidden layers, learning rates, and activation functions. This process is often empirical, requiring iterative experimentation and experience, as there is no definitive rule for determining the best configuration. Training deep neural networks can be computationally intensive, necessitating substantial processing power and memory. This demand has led to development and utilization of specified hardware accelerators, such as Graphics Processing Units (GPUs) and Tensor Processing Units (TPUs), to expedite training processes. Despite these advancements, the computational cost remains a significant consideration, especially for large-scale models. Another limitation of ANNs is their generalization capability. While they can perform well on data similar to their training set, their performance may degrade after applied to data with diverse geometries or boundary conditions. This issue is particularly pertinent in fields like fluid dynamics, where difficulties often include complex geometries and varying circumstances. In such cases, retraining or adapting the network to new scenarios is necessary to maintain accuracy.

This study uses the LMANN, which incorporates the projected ANN, to forecast the behavior of mixed convection hybrid nanofluid flow with nanoparticles (TiO_2+CuO) and H_2O a base fluid traveling through a cylinder/plate. Moreover, weight modifications are utilized to leverage the yield objective's dependencies and connections. For accurate predictions, the ANN model requires thorough optimization. Figure 7 depicts the outputs of the activation function, ranging from 1 to 0. This function has a smooth, S-shaped behavior, but is not linear, with two hidden layers comprising 11 neurons and one output layer containing 9 neurons.

Lagaris et al.[30] introduced a method for constructing trial solutions to differential equations by decomposing the solution into two components: the first inherently satisfies the boundary conditions, while the second, parameterized by a neural network, is trained to fulfill the differential equation itself. This approach necessitates identifying an initial function that meets the boundary conditions, which can be a complex task. To address this, Piscopo et al.[42] proposed an alternative strategy wherein boundary conditions are incorporated directly

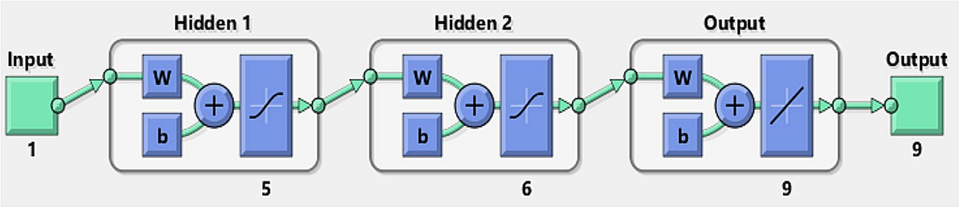

Fig. 7. ANN design for the proposed model.

into the loss function as penalty terms. In this framework, the ANNs' yield serves as the trial resolution, and the loss function quantifies the discrepancy between the network's prediction and the desired solution, typically using the squared difference. Training includes adjusting weights and biases of FFNN to decrease this loss, thereby enhancing the exactness of the explanation. This process intends to reduce faults encountered when transitioning from the initial trial solution to the final, optimized solution:

$$\tilde{f}x = \frac{1}{1 + \exp -x} \tag{23}$$

Improving network performance is the next step for ANN approaches. The MSE and coefficient of determination (R-value) formulae are as follows:

$$MSE = \frac{1}{n}\sum_{i \geq n} X_{e^i} - X_{ANNi}2, \tag{24}$$

$$R = \sqrt{1 - \frac{\sum_{i \geq n} X_{e^i} - X_{ANNi}2}{\sum_{i \geq n} X_{e^i}2}}, \tag{25}$$

Moreover, by juxtaposing the presumed and intended data, the error rate estimates might facilitate the evaluation of the accuracy of the ANN design.

$$\% \, Error\ rate = \frac{X_{\exp} - X_{ANNi}}{X_{\exp}} \times 100 \tag{26}$$

The optimization procedure calculates gradients of loss function regarding network parameters. Utilizing the whole training dataset guarantees the continuous incorporation of boundary conditions after respectively modernization of network parameters. Our NN design has double hidden layers using the sigmoid activation function. We use the ADAM optimizer[43] to optimize the network parameters, initializing it with a learning rate of 0.0001.

Graphical representation of data distribution

The current research work emphasizes simulation-based training of ANNs based on the LMA and offers a comparative analysis of the resultant numerical results. For this, a dataset is produced with the help of the numerical solver of boundary value problems, bvp4c, and the same is utilized as the starting input for training the LMA-inspired neural network (LMANN). It takes a supervised learning approach through the implementation of a feedforward neural network with three layers, including input, hidden, and output. The data are separated to achieve model generalizability and model performance evaluation, where 80% is utilized in training, 10% is utilized in validating, and another 10% is utilized for testing. The graphical representation of such partitioned data, as shown in Fig. 8, highlights the learning behavior of the network, speed of convergence, and predictive accuracy. From the visualization, one can also learn about the efficiency with which the ANN learns the nonlinear patterns of such data generated from bvp4c, indicating the effectiveness of LMA in reducing the training error and improving model robustness.

Results and discussion

This part has produced physics behind the graphical outputs about the change in physical parameters affecting velocity, temperature profile, and mass transfer. Figures 9, 10, 11 and 12 show the results of the porosity parameter $(0.1 \leq Pm \leq 0.5)$, mixed convection parameter $(0.5 \leq \gamma \leq 1.5)$, inclination angle factor $(0^\circ \leq \beta \leq 90^\circ)$, CuO–TiO$_2$–NPs$(0.0 \leq \phi_1 = \phi_2 \leq 0.025)$, thermal-Biot number $(0.10 \leq \lambda \leq 0.16)$, homogeneous reaction $(0.1 \leq L1 \leq 0.7 \leq L1 \leq 0.7 \leq L1 \leq 0.7 \leq L1 \leq 0.7 \leq L1 \leq 0.7 \leq L1 \leq 0.7)$, heterogeneous reaction $(0.3 \leq Ls \leq 0.9 \leq Ls \leq 0.9 \leq Ls \leq 0.9 \leq Ls \leq 0.9 \leq Ls \leq 0.9 \leq Ls \leq 0.9)$, heat source/sink parameter $(0.1 \leq Qe \leq 0.5)$, Thermal radiation parameter $(0.20 \leq Rd \leq 0.30)$, Schmidt number $(0.1 \leq Sc \leq 0.3)$, velocity profile $(f'(\zeta))$, Mass profile $(h(\zeta))$, and temperature profile $(\theta(\zeta))$.

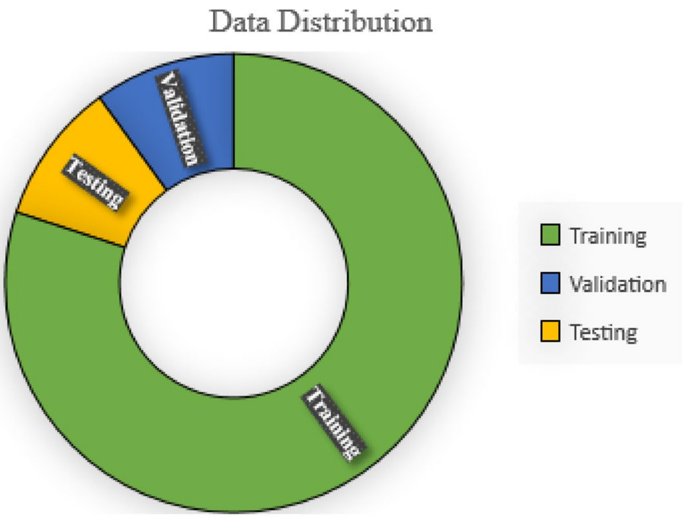

Fig. 8. ANN-data distribution.

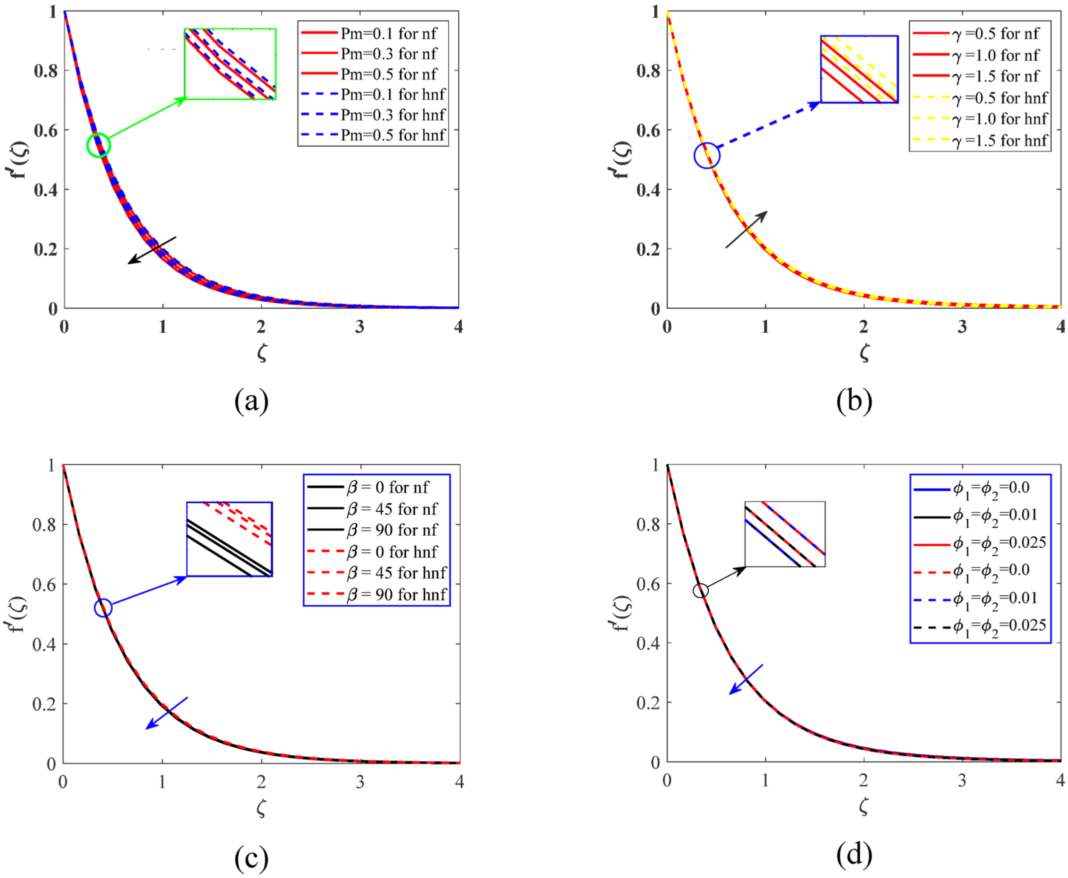

(a) (b)

(c) (d)

Fig. 9. Variation of velocity profile with (**a**) porosity parameter, (**b**) mixed convection parameter, (**c**) inclination angle, and (**d**) nanoparticle concentration. Higher porosity and inclination reduce velocity due to increased resistance, while stronger buoyancy enhances flow.

The impression of porosity parameter (Pm) on $f'(\zeta)$ is seen in Fig. 9a. As the intensity of Pm increases, the HNF velocity curve decreases. Physically, the primary reasons for the reduction in fluid velocity brought on by greater Pm are reduced saturation and fluid retention in open pores. These elements hinder fluid flow and reduce its speed. Figure 9b shows that the velocity curve $f'(\zeta)$ is enhanced by the action of mixed convection

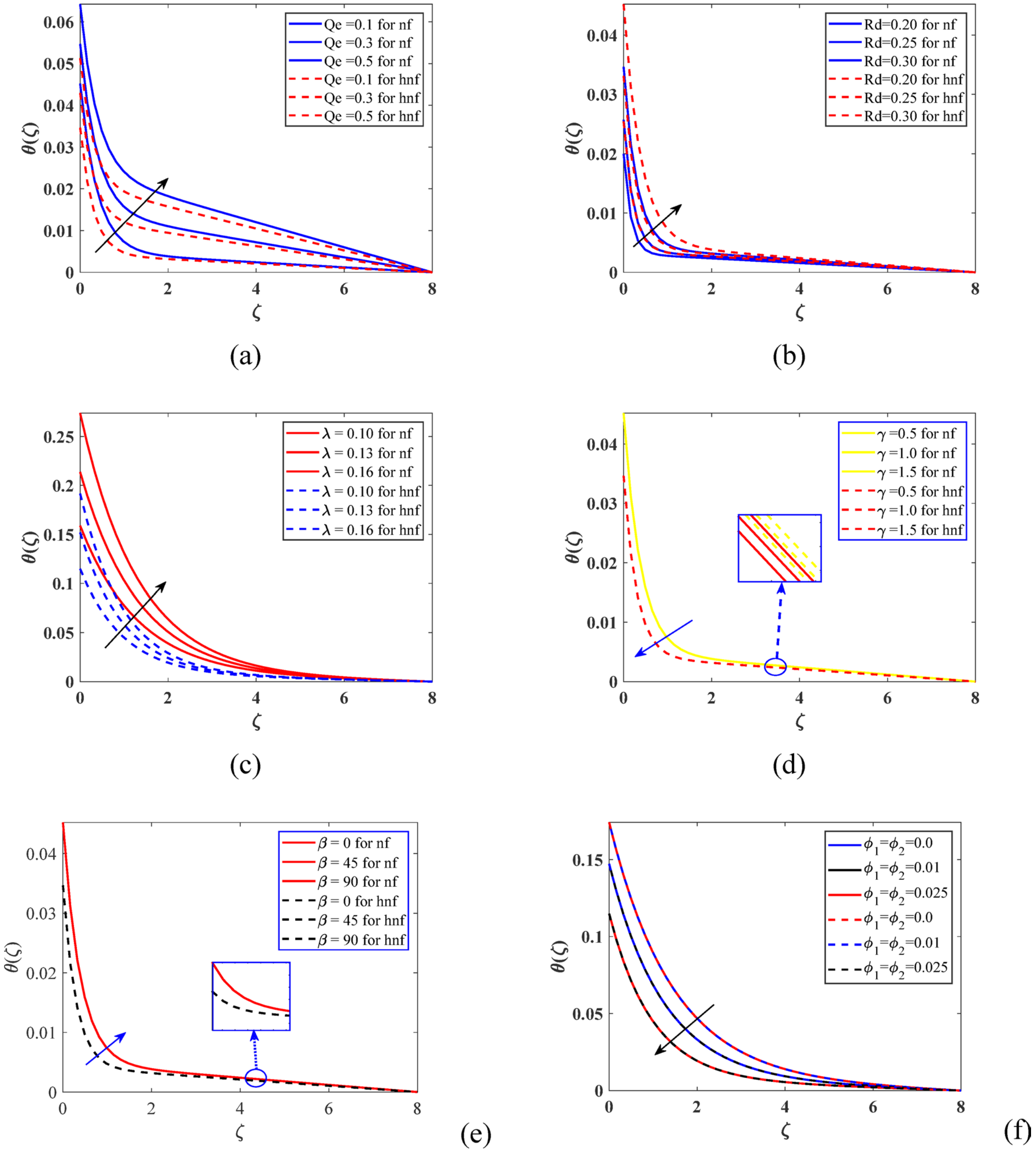

Fig. 10. Variation of temperature profiles with key parameters: (**a**) heat source/sink parameter, (b) thermal radiation parameter, (**c**) Biot number, (**d**) mixed convection parameter, (**e**) inclination angle, and (**f**) nanoparticle concentration. Heat source/sink and radiation enhance the fluid temperature, while higher Biot number increases surface heat resistance. Inclination angle raises thermal energy due to gravity effects, whereas higher nanoparticle loading improves heat dissipation, lowering the temperature.

(γ).Physically, the increasing influence of γ designates that fluid flow is increasingly affected by resistant forces. The velocity curve increases when γ becomes significant. The velocity curve is improved due to fluid motion being driven by the γ. The impression of inclination angle factor on $f'(\zeta)$ is seen in Fig. 9c. It has been observed that the velocity curve decreases as the cylinder or plate angle increases from 0° to 90°. The increasing values of β that oppose fluid movement are the cause of the gravitational pull. The pressure gradient across the stream may be altered by β. As the flow encounters various forms of resistance in different directions, this altered pressure distribution may cause the fluid velocity to drop. The impact of CuO–TiO$_2$–NPs on $f'(\zeta)$ is seen in Fig. 9d. It is obvious that when concentration of CuO–TiO$_2$–NPs increases, the fluid velocity decreases. In terms of physics, $\phi_1 = \phi_2$ typically have superior thermal conductivities than the base fluid. The average thermal conductivity of the nanofluid is enhanced by these NPs. The resulting increased thermal conductivity allows for a more efficient heat exchange over the HNF, which speeds up cooling and lowers fluid velocity.

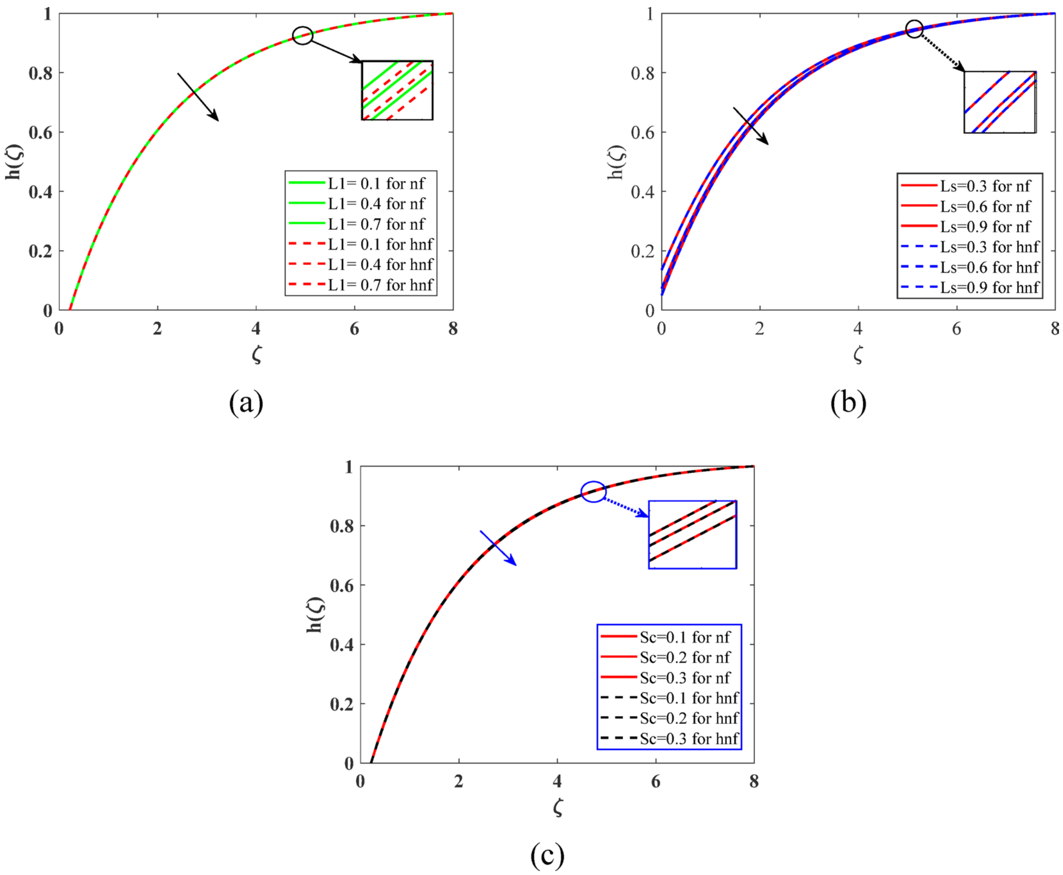

(a) (b)

(c)

Fig. 11. Mass concentration profiles for (**a**) homogeneous reaction, (**b**) heterogeneous reaction, and (**c**) Schmidt number. Both homogeneous and heterogeneous reactions reduce concentration as reactants are consumed during the process, while higher Schmidt number suppresses diffusion, leading to thinner concentration boundary layers.

The effects of Qe and Rd on fluid temperature are seen in Figs. 10a and b. As Qe and Rd parameters increase, more heat is physically delivered into the fluid. The fluid's total temperature rises as a result of the additional heat energy it absorbs from source. Figure 10c shows how temperature profile $(\theta(\zeta))$ is affected by thermal Biot number (λ). Physically, the Biot number establishes a relationship between the rate of heat conduction inside a fluid and the rate of energy distribution at the surface of a cylinder or plate. The influence of thermal Biot number causes the fluid's temperature to rise because inactive rate of heat transmission over the plate or cylinder surface keeps the heat from rapidly absorbing or dispersing. Figure 10d illustrates how the mixed convection parameter affects the $\theta(\zeta)$. The result of γ has been shown to decrease the $\theta(\zeta)$. In terms of physics, the increasing impact of γ indicates that buoyant forces have a greater influence on fluid temperature and flow. As the buoyancy force increases, the velocity curve rises in importance. The fluid motion is driven by buoyancy forces, which cause the energy profile $\theta(\zeta)$ to decrease and the velocity to increase.

Figure 10e shows that when the mounting upshot of (β) grows, so does the energy field of HNF. Gravity has an impact on the temperature fluctuation of a fluid passing through an inclined surface. As the fluid moves upward, potential energy is converted to kinetic energy, and mechanical energy is rehabilitated to thermal energy by friction and turbulence, raising the fluid's temperature. The impact of CuO–TiO_2–NPs on the HNF thermal profile is seen in Fig. 10f. In terms of physics,CuO–TiO_2–NPs typically have higher thermal conductivities than the base fluid. The average thermal conductivity of the nanofluid is enhanced by these NPs. The resulting increased thermal conductivity allows for a more efficient heat exchange across the HNF, resulting in faster cooling and a temperature decrease. Furthermore, the addition of NPs can improve the heat dissipation properties. $\phi_1 = \phi_2$ are better at absorbing and transferring heat. The fluid's thermal profile decreases as a result of its increased ability to dissipate heat.

The characteristics of mass profile $h(\zeta)$ in relation to homogeneous reaction $L1$, heterogeneous reaction Ls, and Schmidt number Sc are shown in Fig. 11a–c, respectively. In a homogeneous reaction, each reactant is uniformly integrated at atomic level. As the reaction progresses, the amounts of reactants and by crops change throughout fluid. Depending on whether the reaction uses reactants or produces products, the concentration of these species decreases or increases along the streams. This could lead to a decline in concentration curve $h(\zeta)$ as reaction proceeds (Fig. 11a). In a heterogeneous reaction, at least one responding mediator is not in the same phase as other reactants, which might be solid, liquid, or gas. These reactions usually occur at interfaces, such

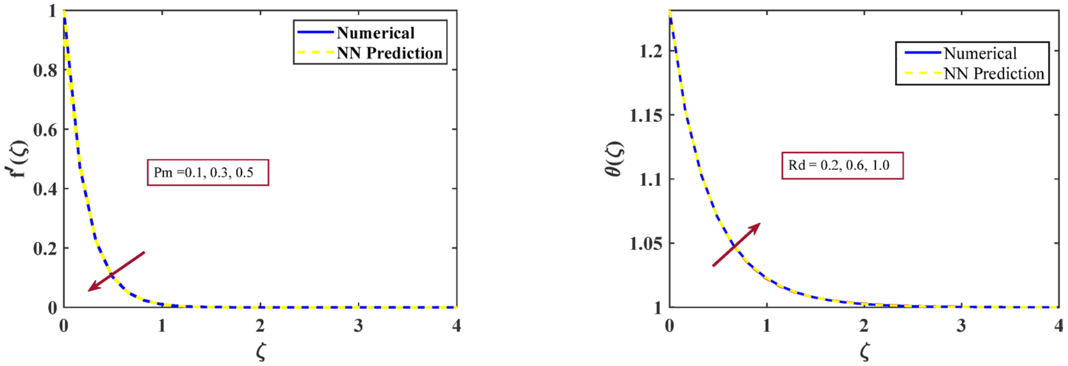

(a) Compression for Case 1

(b) Compression for Case 2

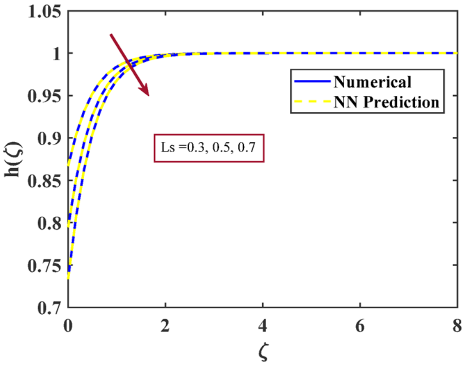

(c) Compression for Case 3

Fig. 12. Comparison of numerical (bvp4c) and ANN results for (**a**) porosity parameter, (**b**) thermal radiation parameter, and (**c**) heterogeneous reaction parameter. In all cases, the ANN predictions show excellent agreement with numerical solutions, demonstrating high fidelity of the trained network across different parameter ranges.

Parameter set	References	Skin friction (C_f)	Nusselt number (Nu)	Sherwood number (Sh)
$\mathrm{Pr} = 6.2,\ Sc = 2.0,\ Rd = 0.5$	Pooja et al.[37]	0.4821	1.236	0.924
	Madhukesh et al.[38]	0.4819	1.234	0.926
	Present study	0.4820	1.235	0.925
$\mathrm{Pr} = 7.0,\ Sc = 1.5,\ Rd = 1.0$	Pooja et al.[37]	0.5623	1.642	1.103
	Madhukesh et al.[38]	0.5620	1.641	1.104
	Present study	0.5622	1.642	1.104

Table 4. Benchmark comparison table.

as when reactants stick to a solid catalyst's outermost layer. As the reaction takes place on surface, the amount of reactants in the larger volume of fluid decreases because they have been used there. This might lead to a reduction in the concentration profile $h(\zeta)$ as reaction proceeds (Fig. 11b). Additionally, Fig. 11c shows that when Sc varies, the mass curve decreases. The molecular diffusivity falls off with the effect of Sc, whereas the kinetic viscosity of a fluid is enhanced, this results in the declination of the mass curve $h(\zeta)$.

Validation of the method

In order to ensure accuracy of the present numerical scheme, our findings were compared with those of Pooja et al.[37] and Madhukesh et al.[38], which are familiar benchmark research studies on HNF flow with homogeneous/heterogeneous reactions. The comparison is presented in Table 4 for skin friction coefficient, Nusselt number, and Sherwood number. The comparison is observed to be in excellent agreement, which justifies the accuracy and validity of the present methodology.

Comparison between plate and cylinder geometries

Since the present study includes plate and cylinder geometries, a direct quantitative comparison of the two cases is helpful. The skin friction coefficient, Nusselt number, and Sherwood number for some chosen sets of parameters are listed in Table 5. Through the results, it can be seen that the cylinder geometry enhances heat and mass transfer over the flat plate because of curvature-induced boundary layer thinning.

Artificial neural networks modelling

ANNs are advanced computational methodologies that forecast various physical attributes of prevalent issues, grounded in the premise that human brain functions as an interconnected network of neural cells. The ANN-LMA technique is well-suited for effectively managing the complexity of our investigation, since it excels in nonlinear optimization (Toghraie et al.[44], Ali et al.[45]). Moreover, it demonstrates the efficacy of ANN training in aligning with the bvp4c, a suggested numerical method. The ADAM optimizer's renowned variable learning rate and momentum render it suitable for various deep learning challenges, including this particular case (Bairagi et al.[46], Karmakar et al.[47]).

The internal neural architecture includes the weight configuration, an output layer including 9 neurons, a first hidden layer with 5 neurons, a second hidden layer containing 6 neurons, and an input layer featuring a single neuron, along with the internal architecture of both input and output layers. Biases enable model to interpret the output of the activation function, facilitating learning and data fitting while identifying nuanced relationships. In contrast, weights in neural networks represent the strength of connections between neurons and assess the significance of input information. The weights and biases acquired during training are essential for the testing and validation of neural networks. They clarify the process by which incoming data is mapped, enabling the model to precisely forecast unknown data. Figures 12, 13, 14 and 15 illustrate the validations for the various parameters utilized in the ANN analysis.

To emphasize the AI-powered prediction aspect of this work, Fig. 12a illustrates the outcomes of the ANN and bvp4c methodologies for various standards of porosity parameter. The ANN model's ability to accurately replicate bvp4c method outcomes across a broad range of values is evident. Furthermore, note the decrease in velocity as the porosity parameter increases. This indicates that Pm significantly influences the system's performance, as accurately demonstrated by both methods. Figure 12b illustrates the outcomes of the ANN and bvp4c methodologies for different thermal radiation values. The ANN model demonstrates a capacity to accurately replicate the outputs of the bvp4c approach across a wide field of values. Furthermore, observe the enhancement in the temperature gradient as it rises. This indicates that the heat radiation parameter significantly affects system performance, as both approaches effectively demonstrate. Figure 12c illustrates the outcomes of the ANN and bvp4c methods for different heterogeneous reaction values. The ANN model reproduces the results of bvp4c approach across a wide range of values. Moreover, observe the reduction in the $h(\zeta)$ as it increases. This demonstrates that, as both techniques imply, the Ls significantly influences system behavior.

Figure 13a–e show the different results of LMA-ANN for the different values of porosity parameter. Figure 13a exemplifies the convergence of MSE for the training dataset. The optimal MSE training results were seen at 1144 epochs, yielding equal values of 2.5304×10^{-09}. Figure 13b demonstrates that at the 1144th epoch, LMA-ANN exhibited gradients of 9.9906×10^{-08}, with Mu 1.0×10^{-08} parameters set at 1144 each. Figure 13c presents histogram graphs with zero error with 20 bins, where the error is equal to the targets and output. For optimal outcomes with LMA-ANN, Fig. 13d depicts the function fit graph, which demonstrates a seamless model, while Fig. 13e presents regression analyses for regression evaluation. The ANN regression results are extremely efficient. For each of the four graphs (training, validation, test, and total), the output values closely track the target line $(Y = T)$, reflecting high prediction efficiency. The points are tightly clustered around the diagonal, which shows R-values ranging from $0.995 - 1.000$ and extremely small error values. This confirms that the ANN model is a good generalizer and predicts with high accuracy.

Figure 14a–e illustrate the varying outcomes of LMA-ANN corresponding to different thermal radiation values. Figure 14a illustrates the convergence of mean squared error (MSE) for the training dataset. The optimal MSE training outcomes were identified at 785 epochs, yielding a value of 6.1869×10^{-10}. Figure 14b indicates that during the 785th epoch, LMA-ANN had a gradient of 9.966×10^{-08}, with Mu values of 1.0×10^{-09}. Figure 14c displays histogram graphs including 20 bins. Figure 14d validates the function fit graph for case 2, demonstrating optimal results achieved with LMA-ANN. Figure 14e presents correlation studies for regression analysis. The ANN regression outcomes are effective. Each of the four graphs (training, validation, test, and total) demonstrates that the output values closely align with the goal line $(Y = T)$, indicating good predictive accuracy. The data points are closely grouped along the diagonal, indicating R-values of 1.000, accompanied by minimal error values. This verifies that the ANN model demonstrates effective generalization and achieves high predictive accuracy.

Figure 15a–e exhibit the varied LMA-ANN outputs for different heterogeneous reaction values. Figure 15a illustrates the convergence of the training dataset's mean squared error (MSE). The most significant results of MSE training were observed during the 339th epoch, with a value of 1.1897×10^{-09}. Figure 15b demonstrates

Parameters $(M,\ \Pr,\ Sc,\ \lambda)$	Geometry	Skin friction (C_f)	Nusselt number (Nu)	Sherwood number (Sh)
(1, 6.2, 2, 0.5)	Plate	0.4820	1.235	0.925
	Cylinder	0.4953	1.271	0.933
(2, 6.2, 2, 1.0)	Plate	0.5622	1.642	1.104
	Cylinder	0.5786	1.685	1.115

Table 5. Plate vs. cylinder comparison of skin friction, Nusselt, and Sherwood numbers, highlighting curvature-induced enhancement in heat and mass transfer.

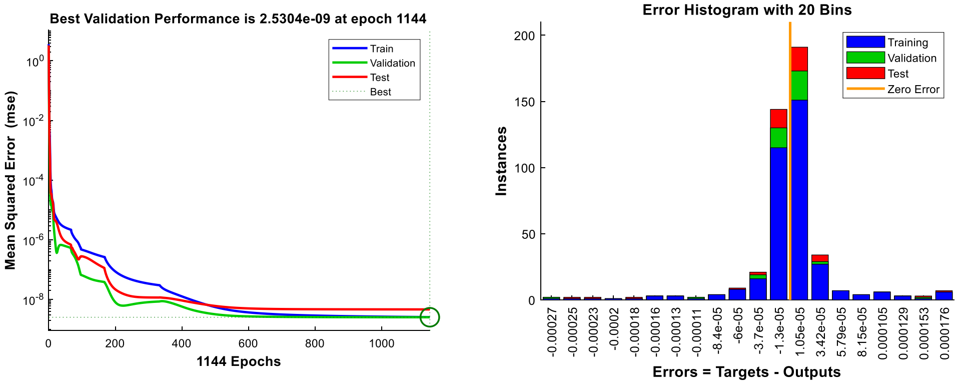

(a) MSE for Case 1

(c) Error Histogram for Case 1

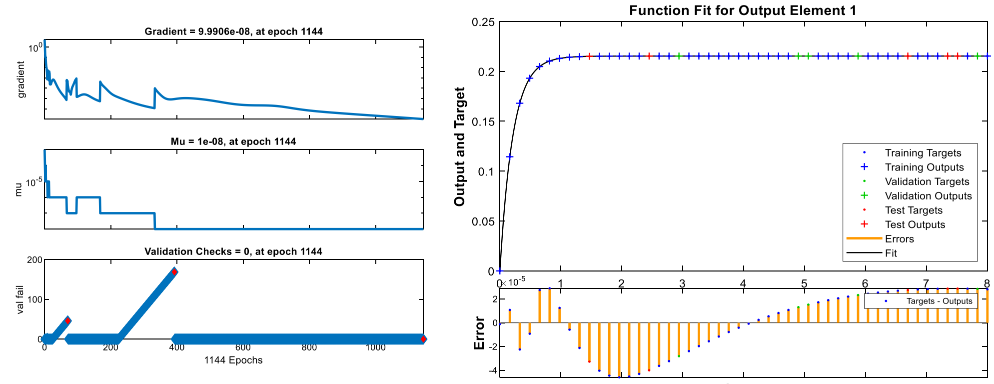

(b)Training state for Case 1

(d) Function Fit for Case 1

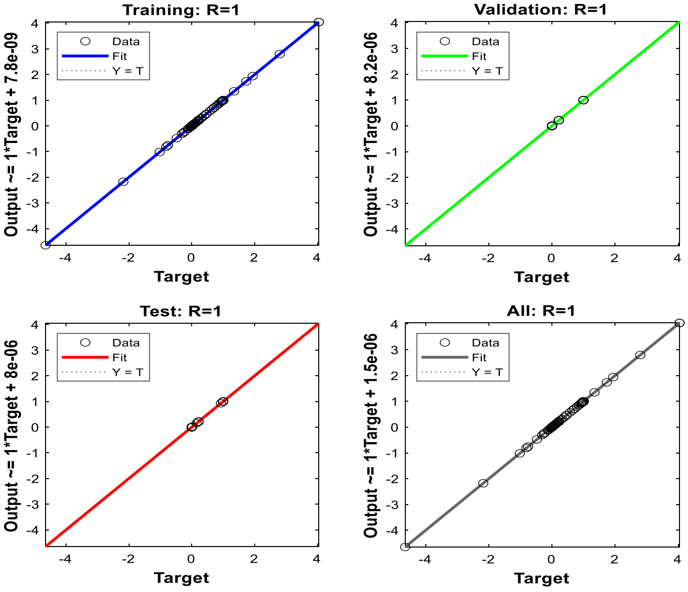

(e) Regression for Case 1

Fig. 13. ANN training and validation performance for porosity parameter: (**a**) mean squared error convergence, (**b**) training state with gradient and Mu evolution, (**c**) error histogram showing minimal deviation, (**d**) function fit illustrating strong correspondence between target and predicted data, and (**e**) regression plots with R ≈ 1, confirming high predictive accuracy.

that at the 339th epoch, LMANN had gradients of 9.884×10^{-08} and Mu values of 1.0×10^{-09}. Figure 15c displays histogram plots with 20 bins. Figure 15d correlates the function fit with the optimal results obtained using LMA-ANN for the specified model. Finally, Fig. 15e presents regression analysis and correlation investigations. The results of ANN regression work really well. Good prediction accuracy is shown by the output values' near

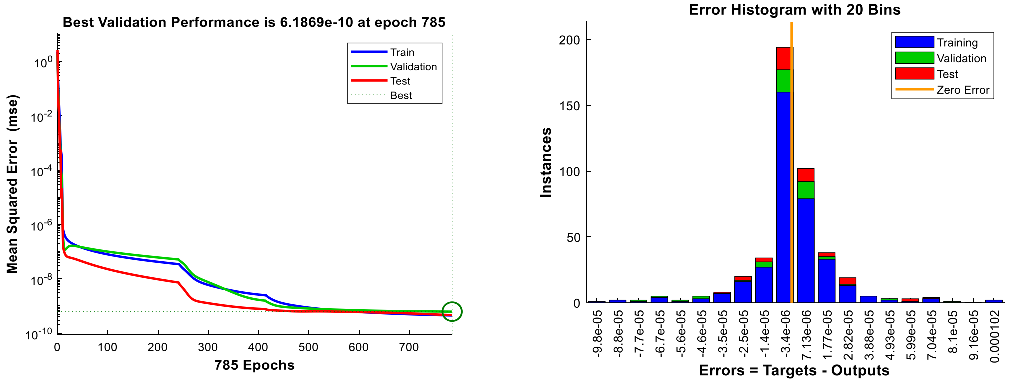

(a) MSE for Case 2

(c) Error Histogram for Case 2

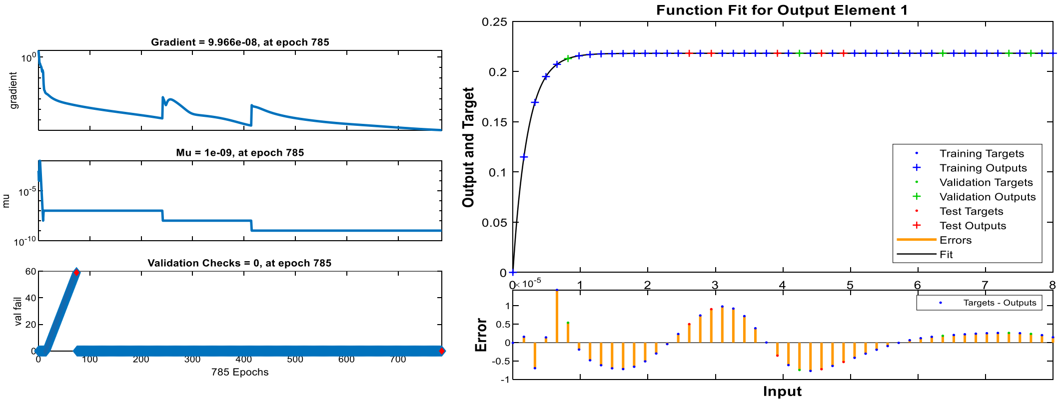

(b) Training state for Case 2

(d) Function Fit for Case 2

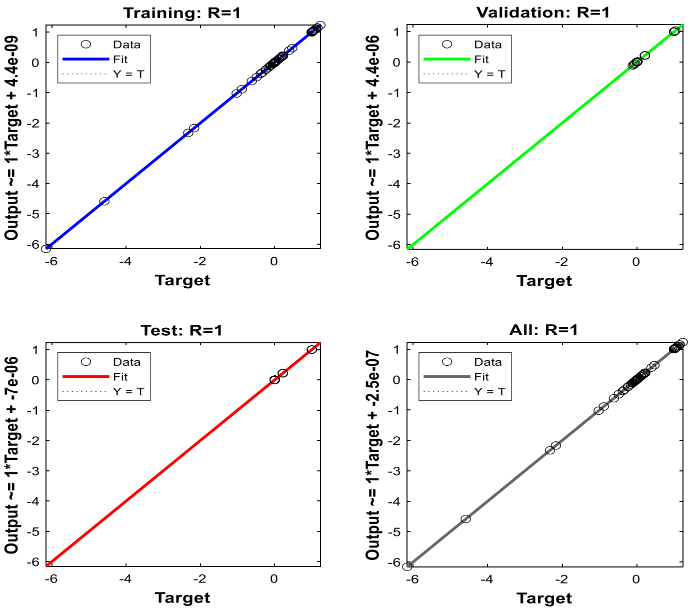

(e) Regression for Case 2

Fig. 14. ANN training and validation performance for thermal radiation parameter: (**a**) convergence of mean squared error, (**b**) training state, (**c**) error histogram, (**d**) function fit, and (**e**) regression analysis. Results confirm stable training and excellent generalization with negligible error.

alignment with the target line $(Y = T)$ in each of the four graphs (training, validation, test, and total). With R-values ranging from 0.996 to 1.000 and low error values, the data points are densely clustered along the diagonal. This confirms that the ANN model has good prediction accuracy and exhibits excellent generalization.

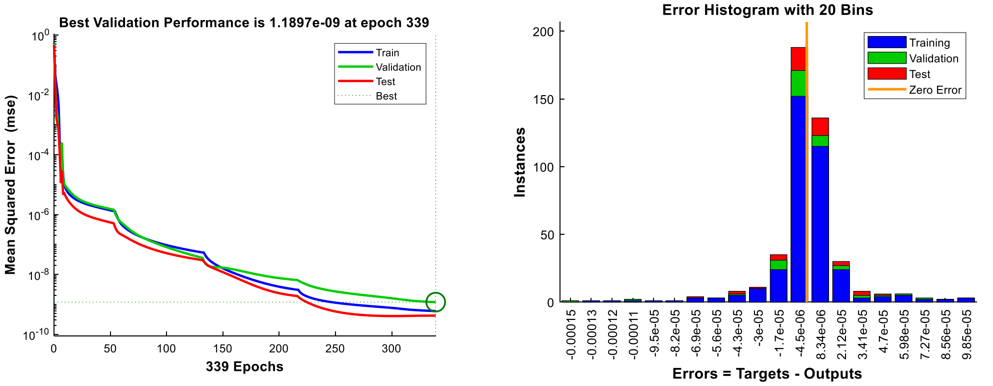

(a) MSE for Case 3
(c) Error Histogram for Case 3

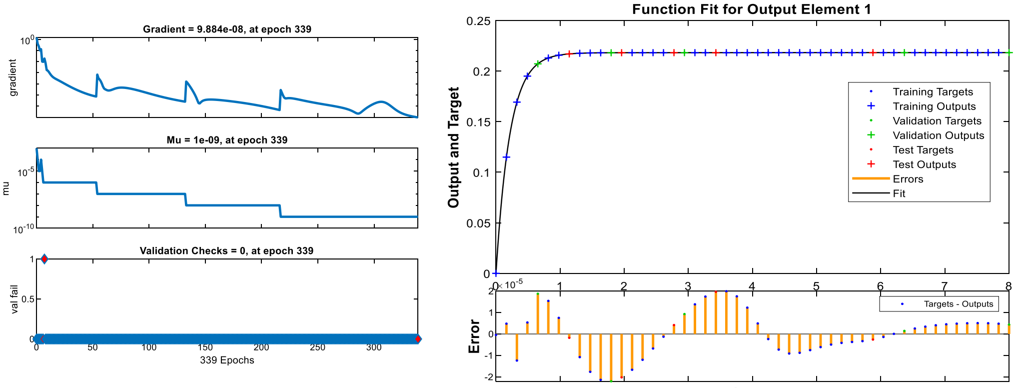

(b) Training state for Case 3
(d) Function Fit for Case 3

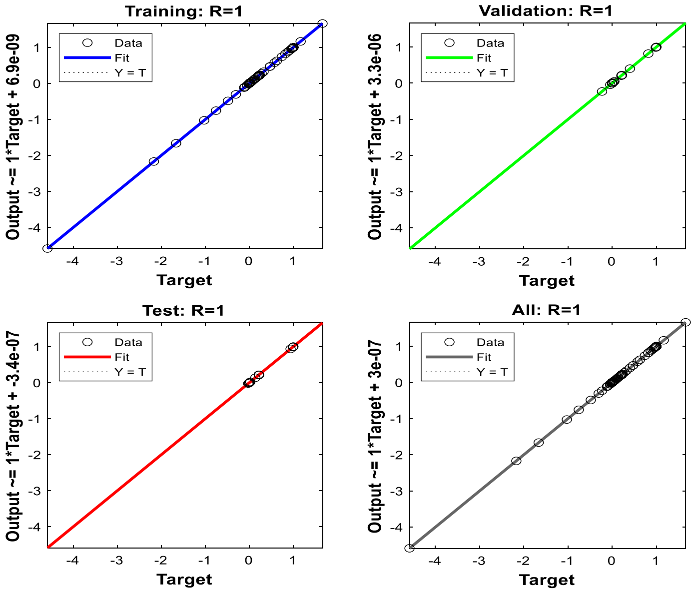

(e) Regression for Case 3

Fig. 15. ANN training and validation performance for heterogeneous reaction parameter: (**a**) mean squared error evolution, (**b**) training state, (**c**) error histogram, (**d**) function fit, and (**e**) regression analysis. The ANN demonstrates strong convergence behavior and high accuracy, with R-values close to unity across all datasets.

Conclusion

We have numerically assessed the continuous two-dimensional HNF flow across an motivated permeable plate/cylinder. The HNF flow is scrutinized in context of heterogeneous and homogeneous chemical reactions, as well as permeable media. The HNF is synthesized using CuO and TiO_2 nanoparticles in water. The transfer of energy in fluid dynamics is formally characterized by an associated nonlinear system of PDEs. The organization of PDEs is reduced to a dimensionless form of ODEs, which are then analyzed numerically using MATLAB function bvp4c. The LMA-ANN training, in conjunction with numerical methods, forecasts flow parameters that affect fluid flow characteristics. A comparison analysis is conducted between the numerical scheme and the ANN to elucidate the consequences. The key conclusions are:

- The influence of porosity parameter (Pm) and the inclination angle factor reduces the velocity curve $f'(\zeta)$ in both the cylinder and plate scenarios. The increasing quantities of CuO–TiO_2–NPs likewise reduce the velocity field. The impact of γ and increasing concentrations of CuO–TiO_2–NPs diminishes the energy field of HNF.
- The impact of Qe and Rd elevates the fluid temperature. The fluid temperature increases owing to the enhancing influence of λ and the angle of inclination parameter.
- The LMA-ANN approach yields predictions with an MSE range of 10^{-08} to 10^{-10} concerning numerical data. The histogram, regression, and function fit analyses of LMA-ANN, together with numerical and graphical representations of MSE convergence plots, validate the accuracy of the numerical approach, and the LMA-ANN data exhibited remarkable concordance with the numerical data.
- The AI-powered ANN predictions demonstrate excellent agreement with numerical results, with negligible errors, confirming the robustness of the proposed hybrid approach.

Limitations

- The study is limited to two-dimensional steady-state flow, not including three-dimensional or transient effects.
- Particular nanoparticles and base fluids were taken into account; one may choose other particles for further studies.
- The chemical reaction models are hypothetical and do not necessarily reflect real-life reaction complexities.
- The LMA-ANN model was trained on a limited parameter range, which can affect its generalizability to broader conditions.
- Spherical nanoparticle correlations for thermophysical properties have been used in the present model. Non-spherical or lattice-type particle structure could lead to quantitative differences, and their consideration will be taken care of in future studies.

Future work

This work provides various directions for further investigations. Important considerations for possible additions are enumerated here:

- Extend the analysis to three-dimensional and unsteady (time-dependent) hybrid nanofluid flows.
- Investigate the performance of different nanoparticles and base fluids. Incorporate more realistic and complex chemical reaction kinetics into the model.
- Investigate non-Newtonian fluid models for more realistic applications. Improve ANN predictions using deep learning techniques and bigger, more varied datasets.
- Introduce uncertainty quantification into ANN modeling for enhanced robustness. Perform experimental verification to support and validate the numerical and ANN findings.

Data availability

Data is provided within the manuscript.

Received: 13 August 2025; Accepted: 18 September 2025

References

1. Sus, C. Enhancing thermal conductivity of fluids with nanoparticles, developments and applications of non-Newtonian flows. *ASME, FED, MD* **1995**(231), 99-I05 (1995).
2. Hayat, T., Muhammad, T., Shehzad, S. A. & Alsaedi, A. On magnetohydrodynamic flow of nanofluid due to a rotating disk with slip effect: A numerical study. *Comput. Methods Appl. Mech. Eng.* **315**, 467–477 (2017).
3. Buongiorno, J. Convective transport in nanofluids. *J. Heat Mass Transf.* **128**(3), 240–250 (2006).
4. Madhukesh, J. K., Ramesh, G. K. & Revadakundi, Y. B. Thermal transport analysis of ternary hybrid nanofluid flow over a vertical cylinder with thermal radiation and chemical reaction. *Therm. Adv.* **3**, 100040 (2025).
5. Yasmin, H., Lone, S. A., Anwar, S., Shahab, S. & Saeed, A. Numerical calculation of thermal radiative boundary layer nanofluid flow across an extending inclined cylinder. *Symmetry* **15**(7), 1424 (2023).
6. Gupta, S., Jangid, N. K., Jain, D., Singhal, V. K. & Jain, C. P. Investigation of radiative MHD Carreau nanofluid over an inclined stretching cylinder with activating energy, Wu's slip, and convective heating. *Numer. Heat Transf. Part B: Fundam.* **85**(1), 1–19 (2024).
7. Salahuddin, T., Tariq, S., Khan, M. & Altanji, M. The impact of Carreau-Yasuda nanofluid flow on ciliated walls of the channel. *Tribol. Int.* **191**, 109152 (2024).
8. Chinnasamy, P. et al. Peristaltic transport of Sutterby nanofluid flow in an inclined tapered channel with an artificial neural network model and biomedical engineering application. *Sci. Rep.* **14**(1), 555 (2024).

9. Saha, T., Saha, G., Parveen, N. & Islam, T. Unsteady magneto-hydrodynamic behavior of TiO_2-kerosene nanofluid flow in wavy octagonal cavity. *Int. J. Thermofluids* **21**, 100530 (2024).
10. Upreti, H., Pandey, A. K., Joshi, N. & Makinde, O. D. Thermodynamics and heat transfer analysis of magnetized Casson hybrid nanofluid flow via a Riga plate with thermal radiation. *J. Computat. Biophys. Chem.* **22**(03), 321–334 (2023).
11. Wang, F. et al. Unsteady thermal transport flow of Casson nanofluids with generalized Mittag-Leffler kernel of Prabhakar's type. *J. Market. Res.* **14**, 1292–1300 (2021).
12. Wang, F., Animasaun, I. L., Obideyi, B. D., Fatunmbi, E. O. & Muhammad, T. Insight into the variations of concentration experiencing leading-edge accretion and thermal analysis: water conveying nanotubes, graphene, and aluminum oxide nanoparticles over a convectively heated surface. *J. Therm. Anal. Calorim.* **149**(15), 8309–8319 (2024).
13. Fuzhang, W. et al. Inspections of unsteady micropolar nanofluid model over exponentially stretching curved surface with chemical reaction. *Waves Random Complex Med.* **35**(1), 763–784 (2025).
14. Ramesh, G. K., Manjunatha, S., Roopa, G. S. & Chamkha, A. J. Hybrid (ND-Co_3O_4/EG) nanoliquid through a permeable cylinder under homogeneous-heterogeneous reactions and slip effects. *J. Therm. Anal. Calorim.* **146**(3), 1347 (2021).
15. Qi, X. et al. Novel thermal error control strategy for feed drive mechanisms via sintered core heat pipe-cooled moving nut. *Int. J. Therm. Sci.* **219**, 110222 (2026).
16. Qian, Y. et al. Numerical characterization and formation process study of rail light bands in high-speed turnout areas. *Eng. Fail. Anal.* **168**, 109083 (2025).
17. Wei, J. et al. Substrate-less power semiconductor packaging for the potential of recyclability. *IEEE J. Emerg. Select. Top. Power Electron.* **13**(2), 2158–2172 (2025).
18. Rawat, S. K. et al. Insight into the significance of nanoparticle aggregation and non-uniform heat source/sink on titania–ethylene glycol nanofluid flow over a wedge. *Arab. J. Chem.* **16**(7), 104809 (2023).
19. Dinarvand, S. et al. Squeezing flow of aqueous CNTs-Fe_3O_4 hybrid nanofluid through mass-based approach: effect of heat source/sink, nanoparticle shape, and an oblique magnetic field. *Results Eng.* **17**, 100976 (2023).
20. Aslani, K. E., Mahabaleshwar, U. S., Sakanaka, P. H. & Sarris, I. E. Effect of partial slip and radiation on liquid film fluid flow over an unsteady porous stretching sheet with viscous dissipation and heat source/sink. *J. Porous Med.* **24**(11), 1–15 (2021).
21. Reddappa, B. & Geetha, R. Effects of second order chemical reaction on MHD forced convection Cu, Ag, and Fe_3O_4 nanoparticles of Jeffrey Nanofluid over a moving plate in a porous medium in the presence of heat source/sink. *J. Integr. Sci. Technol.* **12**(3), 762–762 (2024).
22. Al-Shammari, H. et al. Heat source/sink impact on wave oscillations of thermal and concentration boundary layer along inclined plate under lower gravitational region. *Case Stud. Therm. Eng.* **53**, 103829 (2024).
23. Mandal, D. K. et al. Thermo-fluidic transport process in a novel M-shaped cavity packed with non-Darcian porous medium and hybrid nanofluid: Application of artificial neural network (ANN). *Phys. Fluids* **34**(3), 033608 (2022).
24. Seawram, S., Nimmanterdwong, P., Sema, T., Piemjaiswang, R. & Chalermsinsuwan, B. Specific heat capacity prediction of hybrid nanofluid using artificial neural network and its heat transfer application. *Energy Rep.* **8**, 8–15 (2022).
25. Ramesh, G. K. et al. Neural network algorithms of a curved Riga sensor in a ternary hybrid nanofluid with chemical reaction and Arrhenius kinetics. *J. Radiat. Res. Appl. Sci.* **17**(4), 101078 (2024).
26. Kumar, P., Almeida, F. & Al-Mdallal, Q. Artificial neural network algorithm for time dependent radiative Casson fluid flow with couple stresses through a microchannel. *Alex. Eng. J.* **125**, 167–184 (2025).
27. Galal, A. M. et al. A besyian regularisation neural network approach for hepatitis B virus spread prediction and immune system therapy model. *Sci. Rep.* **14**(1), 23672 (2024).
28. Butt, Z. I. et al. MHD slip flow through nanofluids for thermal energy storage in solar collectors using radiation and conductivity effects: A novel design sequential quadratic programming-based neuro-evolutionary approach. *Mod. Phys. Lett. B* **39**, 2550075 (2024).
29. Lee, H. & Kang, I. S. Neural algorithm for solving differential equations. *J. Comput. Phys.* **91**(1), 110–131 (1990).
30. Lagaris, I. E., Likas, A. & Fotiadis, D. I. Artificial neural networks for solving ordinary and partial differential equations. *IEEE Trans. Neural Netw.* **9**(5), 987–1000 (1998).
31. Zubair, M., Qureshi, H., Hussain, A., Khan, W. A. & Muhammad, T. Machine learning-based stochastic investigation of heat and momentum transfer in ternary-hybrid nanofluids with aggregation effects using artificial neural networks. *J. Therm. Anal. Calorim.* https://doi.org/10.1007/s10973-025-14419-x (2025).
32. Srinivasacharya, D. & Kumar, R. S. Artificial neural network modeling of the Casson fluid flow over unsteady radially stretching sheet with Soret and Dufour effects. *J. Therm. Anal. Calorim.* **147**(24), 14891–14903 (2022).
33. Qureshi, H. AI-driven analysis of buoyancy-convective flow of ternary-hybrid nanofluid in a porous medium over stretching cylinder. *Nonlinear Dyn.* https://doi.org/10.1007/s11071-025-11620-3 (2025).
34. Mahla, R. & Kaladhar, K. Computational analysis of mixed convection Jeffrey fluid flow between rotating discs: Incorporating magnetic field and thermal radiation via neural network modeling. *Eur. Phys. J. Plus* **139**(4), 344 (2024).
35. Qureshi, H., Latif, A., Athar, T., Raheem, A. & Muhammad, T. Artificial Neural Network Driven Investigation of thermal exchange through hybrid nanofluid of polymer/CNT across parallel sheets. *Case Stud. Therm. Eng.* **74**, 106903 (2025).
36. Butt, Z. I. et al. Radial basis kernel harmony in neural networks for the analysis of MHD Williamson nanofluid flow with thermal radiation and chemical reaction: An evolutionary approach. *Alex. Eng. J.* **103**, 98–120 (2024).
37. Pooja, M. N., Narasimhamurthy, S. K. & Anitha, V. Numerical investigation of flow dynamics of Williamson fluid over an expanding cylinder/plate in presence of homogeneous/heterogeneous reactions. *Int. J. Appl. Comput. Math.* **10**(1), 10 (2024).
38. Madhukesh, J. K. et al. Investigation of thermal performance of ternary hybrid nanofluid flow in a permeable inclined cylinder/plate. *Energies* **16**(6), 2630 (2023).
39. Mahmood, Z. et al. Heat transfer in radiative hybrid nanofluids over moving sheet with porous media and slip conditions: Numerical analysis of variable viscosity and thermal conductivity. *Mater. Today Commun.* **40**, 109664 (2024).
40. Mahmood, A., Aziz, A., Jamshed, W. & Hussain, S. Mathematical model for thermal solar collectors by using magnetohydrodynamic Maxwell nanofluid with slip conditions, thermal radiation and variable thermal conductivity. *Results in Phys.* **7**, 3425–3433 (2017).
41. Ahmed, S. E., Hussein, A. K., Mansour, M. A., Raizah, Z. A. & Zhang, X. MHD mixed convection in trapezoidal enclosures filled with micropolar nanofluids. *Nanosci. Technol. Int. J.* https://doi.org/10.1615/NanoSciTechnolIntJ.2018026118 (2018).
42. Piscopo, M. L., Spannowsky, M. & Waite, P. Solving differential equations with neural networks: Applications to the calculation of cosmological phase transitions. *Phys. Rev. D* **100**(1), 016002 (2019).
43. Kingma, D. P., & Ba, J. Adam: A method for stochastic optimization. *arXiv preprint* arXiv:1412.6980. (2014).
44. Esfe, M. H., Toghraie, D. & Amoozadkhalili, F. Optimization and design of ANN with Levenberg-Marquardt algorithm to increase the accuracy in predicting the viscosity of SAE40 oil-based hybrid nano-lubricant. *Powder Technol.* **415**, 118097 (2023).
45. Ali, F. et al. Intelligent computing with Levenberg–Marquardt artificial neural network for Carbon nanotubes-water between stretchable rotating disks. *Sci. Rep.* **13**(1), 3901 (2023).
46. Bairagi, T., Hasan, M. J., Hudha, M. N., Azad, A. K. & Rahman, M. M. Artificial neural network (ANN) analysis on thermophysical properties of magnetohydrodynamics flow with radiation in an arc-shaped enclosure with a rotating cylinder. *Heliyon* **10**(7), e28609 (2024).
47. Karmakar, P., Das, S., Mahato, N., Ali, A. & Jana, R. N. Dynamics prediction using an artificial neural network for a weakly conductive ionized fluid streamed over a vibrating electromagnetic plate. *Eur. Phys. J. Plus* **139**(5), 407 (2024).

Acknowledgements

The authors are grateful to King Saud University, Riyadh, Saudi Arabia, for funding this work through the Ongoing Research Funding program—Research Chairs (ORF-RC-2025-0130).

Author contributions

Muhammad Imran: Conceptualization, investigation, software, writing—original draft, writing—reviews & editing. Wantao Jia: Supervision, validation, writing—original draft. Syed Tauseef Saeed: Investigation, methodology, project administration, supervision. Jihad Younis: Software, validation, writing—original draft. Mubashir Qayyum: Supervision, validation, writing—original draft. Abdulrahman A. Almehizia: Conceptualization, data curation, formal analysis, writing—reviews & editing.

Funding

This research was funded by King Saud University, Riyadh, Saudi Arabia, through the Ongoing Research Funding program - Research Chairs (ORF-RC-2025-0130).

Declarations

Competing interests

The authors declare no competing interests.

Additional information

Correspondence and requests for materials should be addressed to J.Y.

Reprints and permissions information is available at www.nature.com/reprints.

Publisher's note Springer Nature remains neutral with regard to jurisdictional claims in published maps and institutional affiliations.